Accepted for publication in the Physics of Fluids on 20th April 2022

Characterization of two-way coupled thermovibrationally driven particle attractee

Marcello Lappa

Department of Mechanical and Aerospace Engineering, University of Strathclyde, James Weir Building, 75 Montrose Street, Glasgow, G1 1XJ, UK – email: marcello.lappa@strath.ac.uk

Abstract: Following the recent identification of a new category of thermovibrationally-driven particle attractors in dilute fluid-particle systems (M. Lappa, Phys. Fluids, 26(9), 093301 (2014); M. Lappa, Phys. Fluids, 31(7), 073303 (2019) and M. Lappa and T. Burel, Phys. Fluids, 32(5), 053314 (2020)), some effort is provided to develop an integrated framework able to encompass earlier discoveries and account for new effects in a single treatment. In particular, we examine the alterations ('corrugation') that can be induced in the geometrically perfect particle structures pertaining to this class of phenomena as the percentage of dispersed solid mass is progressively increased. The related dynamics are explored within the framework of a two-way coupled model with respect to several parameters (solid mass load, density ratio, frequency and amplitude of the imposed vibrations). Ensuing results are interpreted by separating instantaneous and time-averaged contributions and using some ideas borrowed from the companion theory of bifurcations. We show that the back influence of particles on the carrier flow can lead to a variety of possible paths of evolution. While in some cases the original attractee can be overshadowed by particle-induced turbulence, in other circumstances new aggregates with heretofore unseen morphology show up.

Keywords: Particle dynamics, attractors, turbulence, two-way coupling.

1. Introduction

Fluids with dispersed particles play an important role in numerous contexts. They really stand at the crossroad of fundamental physics (Schwabe and Mizev[1]; Gotoda et al.,[2]; Melnikov and Shevtsova[3]), astrophysics (Adams and Watkins[4]; Lappa[5]), chemistry (Knez et al.,[6]), biology (Wang and Xing[7]; Lappa[8]), materials science (Saeedi et al.,[9]) and thermal and mechanical engineering (Saghir and Mohamed[10]; Aksouh et al.,[11]; Bürger and Wendland[12]). Related problems include (but are not limited to) fluid-dynamic instabilities in complex fluids (Matas et al.,[13]; Lashgari et al.,[14]; Lappa[15]), the interaction of an immiscible phase with turbulent flow (Eaton and Fessler[16]; Saw[17]; Bragg[18]; Shim and You[19]), particle ordering in laminar convection (Yarin et al., [20]; Tanaka et al.,[21]; Schwabe et al.,[22]; Ueno et al.,[23]; Pushkin et al.,[24]; Melnikov et al.,[25]; Gotoda et al.,[26]; Toyama et al.,[27]; Lappa[28-31]; Metcalfe,[32] , Venditti et al.,[33]), and the fascinating prospect of using some of these phenomena to produce 'active' matter, i.e. parts or components that can recognize and bind to each other and form well-defined networks or systems[9,5]. Other intriguing directions of research originate from the possibility to interpret theoretically all these behaviors as they were the manifestation in the physical space of complex non-linear dynamics governed by overarching 'attractors' in the phase space ('attractee'). The advantage relating to this point of view obviously lies in the ensuing

process of abstraction, by which specific cases (like the one addressed in the present work) can be used as a testbed for the definition of more general problems or fundamental questions.

In such a context, it is worth highlighting that much attention has been attracted by turbulent flows given their ability to promote particle clustering via different possible routes and because of the myriad technological applications they are relevant to. The underlying mechanisms have been studied over many years (see, e.g., Ref[17] and references therein) together with the tendency of these flow to induce diametrically opposite behaviors, i.e. *particle scattering* (see, e.g., Sommerfeld[34]). Although the variety and dispersion of these results still call for an effort to unify the information to general criteria, more recently, some physicists and engineers have placed their hopes in laminar (deterministic) flows as possible candidates for the identification of new particle attractors. Notably, this specific line of inquiry has succeeded in showing that remarkable exemplars can be found in the category of *simply time-periodic flows* (Lyubimov et al.,[35]; Haller and Sapsis[36]; Lappa[5]; Pushkin et al.,[24]).

As the reader might have realized at this stage, obviously, the final goal of all this research is a more exhaustive (academic) characterization of all these phenomena (and, indeed, relevant theoretical explanations have been elaborated for the ability of particles to self-organize in both turbulent and laminar cases). In particular, it has been clarified that a large part of these mechanisms rely on purely *topological relationships*. While point tracers should in general be considered as mere abstractions, which do not reflect physical reality, real particles have finite size and often different density with respect to the fluid hosting them. For these reasons, their trajectories and the streamlines of the carrier flow *do not overlap exactly*. Since the small departures caused by particle drag, inertial effects and other body forces present in the considered system tend to accumulate, the distribution of particles can undergo significant changes as time elapses. This process can finally result in regions of *clear fluid* (with relatively small or negligible presence of solid matter) and, by contrast, *dense clusters* formed by the spontaneous accumulation of particles. Notably, as this behavior somehow resembles that of a gas undergoing changes in the local density due to significant gradients of velocity (this being often the case in typical problems of compressible aerodynamics), the dynamics of finite-size particles can be assimilated to that of a *compressible medium* (Pushkin et al.,[24] Metcalfe,[32] , Venditti et al.,[33] and references therein).

A typical fingerprint of this class of events in laminar flows is their extremely ordered appearance (as opposed to the fractal morphology of the disordered aggregates induced by turbulent flow). These patterns can display a variable number of dimensions depending on the considered circumstances. As an example, they are essentially one-dimensional (manifesting as a thread of particles) when the time-periodic nature of the carrier flow is due to the propagation of a wave along the axis of a basic roll (Tanaka et al.,[21]; Schwabe et al.,[22]; Pushkin et al.,[24]; Capobianchi and Lappa,[37-38]), or two-dimensional if two counter-propagating waves are present. In the latter case, particles generally accumulate in those regions of the space where the amplitude of disturbance resulting from the combination of the two waves is negligible (Rossing[39], Lappa[31]; Capobianchi and Lappa[40]).

They can take much more complex shapes if the time periodicity of the flow is due to other effects, and this is indeed the case of *thermovibrational convection*, i.e. fluid motion induced in a non-isothermal liquid by the application of vibrations (Gershuni and Lyubimov[41]; Savino and Lappa[42]; Mialdun et al.,[43]; Ahadi and Saghir[44]; Lyubimova et al.,[45]; Bourab et al.,[46]; Shevtsova et al.,[47-48]; Maryshev et al.,[49]; Lappa[50]; Vorobev and Lyubimova[51]; Boaro and Lappa[52-53]; Crewdson and Lappa[54-55]). Interestingly, the study of particles dispersed in a fluid undergoing this type of convection inside a compact cavity has revealed a zoo of particle structures with surprising geometrical perfection (such as cylinders, hyperboloids, ellipsoids and conical surfaces[5,56-59]), which suggests all these dynamics might be governed by hidden (not yet clarified) precise mathematical laws.

Existing numerical works on the subject have added several pieces to this puzzle. It has been understood that the underlying mechanisms are essentially independent of inter-particle forces, i.e. particle-to-particle interactions are not required to justify the existence of attractors. This should be regarded as a notable difference with respect to other aggregates where vibrationally-induced hydrodynamic forces play a crucial role (such as those studied, e.g., by Tabakova and Zapruanov[60]; Wunenburger et al.,[61]; Ivanova et al., [62]; Kozlov et al.,[63]). Attractive forces are not needed because the existence of accumulation loci, all having the shape of 'quadrics', is supported by a delicate phenomenon of synchronization between the inertial response of the dispersed particles to the variable acceleration produced by vibrations and the thermovibrational convective effect *per se*[56-59]. Most remarkably, this specific property allows the emergence of particle structures also in relatively *dilute dispersions*.

As a fleeting glimpse into the existing literature would immediately reveal, the umbrella of on-going research on this specific subject has essentially drawn on studying the influence of asymmetries present in the considered physical system on this synchronization process (*asymmetries due to the shape of container*[57], due to the *direction of vibrations with respect to the walls of the cavity*[58-59], or *asymmetries spontaneously produced due to time-averaged convective effects*,[64] or other mechanisms enabled when the carrier thermovibrational flow displays a certain intrinsic degree of turbulence, Crewdson and Lappa[65]). No analysis has been devoted until now to explore another important question, that is, to what extent these delicate structures can survive in non-dilute fluid-particle mixtures. Given the essentially inertial nature of these phenomena, this is obviously a legitimate question. The *volume fraction of dispersed mass* should be considered as another relevant influential parameter.

In order to address this problem, the present article presents findings that relate to the back influence that particles can exert on the carrier thermovibrational flow when a relative high 'load of mass' is considered (defined as the ratio of the overall solid mass to that of the fluid).

The required theoretical-mathematical two-way coupling framework is elaborated in the following section together with a brief presentation of the main objectives of the overall study.

2. Objectives and Mathematical Model

In order to meet the main goal discussed in the introduction, the intended outcomes of the present analysis are set as follows:

- Develop and validate a generalized model for evolving particles in fluid flow described by a hierarchy of mathematical kernels based on the combination of Eulerian (for fluid flow) and Lagrangian (for particles) approaches, by which different degrees of coupling can be implemented for the solid and liquid phases.
- Expand the space of parameters through explicit consideration of the solid mass load (or particle volume fraction) and perform a parametric study aimed at the identification of particle attractors (the "attractee").
- Determine the regions of this space where, *using the attractors as 'templates'* for the accumulation process, particles can effectively form *recognizable structures*.
- Evaluate the impact of two-way coupling on the morphology and regularity of these structures (including the possible emergence of chaos or turbulence for some specific conditions).

2.1 Geometrical model, particles and vibrational effects

For consistency with earlier studies on the subject where dilute distributions of particles were examined (under the assumption of one-way coupled flow), here we focus on the same archetypal geometrical configuration considered by Lappa[56, 59], namely a differentially heated cubic enclosure undergoing vibrations along a direction perpendicular to the imposed temperature difference (as shown in Fig. 1, temperature difference and vibrations are along the z and y axes, respectively, while x plays the role of 'spanwise direction').

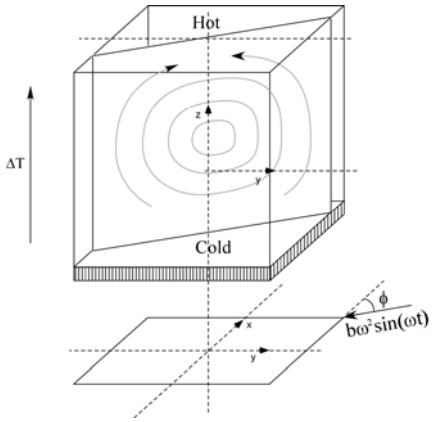

Figure 1: Cubic cavity with characteristic size L, delimited by solid walls (one at z=-0.5 cooled, the other at z=0.5 heated, adiabatic conditions on the remaining sidewalls). The vibrations are parallel to the y axis.

By modeling vibrations through a simple sinusoidal function (Shevtsova et al.,[47,48]), i.e. as $\underline{s}^{lab}(t) = \mathrm{b}\sin(\omega\ \mathrm{t})\underline{\hat{n}}$ (where $\underline{\hat{n}}$ is the unit vector along the direction of shaking, b is the displacement amplitude and $\omega=2\pi f$ is the related angular frequency), the time-varying acceleration affecting the entire system can directly be obtained by taking the second time derivative of $\underline{s}(t)$, that is, $\underline{g}(t) = g_\omega \sin(\omega\ \mathrm{t})\underline{\hat{n}}$. These simple considerations lead to the identification of the first two independent problem variables, namely the frequency ω and amplitude b of imposed vibrations. Of course, other degrees of freedom are represented by the nature of the fluid itself and the applied temperature difference.

As usual, the complexity of the problem can be simplified if it is cast in terms of non-dimensional characteristic numbers. Indeed, in such a framework, the number of influential factors can be greatly reduced. They are the well-known Prandtl number ($\mathrm{Pr}=\nu/\alpha$ where ν is the fluid kinematic viscosity and α its thermal diffusivity) depending on the considered fluid, the nondimensional vibration frequency (Ω), the nondimensional acceleration amplitude (γ) and buoyancy factor (β) defined as:

$$\varpi = \frac{\omega L^2}{\alpha};\ \gamma = \frac{b\omega^2 L^3}{\alpha^2};\ \text{and}\ \beta = (\beta_T \Delta T) \tag{1}$$

where β_T is the fluid thermal expansion coefficient. These parameters can be combined to form alternate characteristic numbers, namely, the classical (vibrational) Rayleigh number (Ra_ω) and the so-called Gershuni number (Gs)

$$Ra_\omega = \gamma\beta/\mathrm{Pr} \tag{2}$$

$$Gs = \frac{(b\omega\beta_T \Delta TL)^2}{2\nu\alpha} = \frac{(\beta_T \Delta TL)^2}{2\nu\alpha}\left(\frac{g_\omega}{\omega}\right)^2 = \frac{1}{2\,\mathrm{Pr}}\left(\frac{\beta\gamma}{\varpi}\right)^2 = \frac{\mathrm{Pr}}{2}\left(\frac{Ra_\omega}{\varpi}\right)^2 \tag{3}$$

The latter plays an important role as it is often used as the characteristic number for the 'mean' (time-averaged) effects in thermovibrational convection, while Ra_ω accounts for the amplitude of the time-varying part[41-42]. Along these lines, it is worth recalling that for the conditions considered in the present work, the velocity of the fluid will consist of two components, one oscillating in time about a mean value equal to zero (the so-called instantaneous velocity) and one steady (corresponding to the velocity averaged over one period of the imposed vibrations), which typically takes a non-zero value. While the former may be considered as a natural consequence of the imposed forcing (the vibrations), the latter should be regarded as a secondary effect produced by the non-linear nature of the governing equations (the Navier-Stokes equations). In general, it is known that if the frequency of vibrations is small, the time-averaged component of velocity is almost negligible, whereas its relative importance with respect to the instantaneous component grows significantly when ϖ is increased. As stated above, the magnitude of these two (oscillatory and

steady) contributions can generally be related to the Rayleigh and Gershuni numbers, as defined by eqs. (2) and (3), respectively.

The dimensionality of the space of parameters obviously further increases when the presence of the dispersed phase is considered. Clearly, it introduces additional degrees of freedom in the considered problem. Two of these degrees clearly relate to the particle radius and density. Relevant independent nondimensional parameters can be defined accordingly as the ratio of the particle to the fluid density,

$$\xi=\rho_P/\rho \tag{4}$$

and the particle Stokes number

$$St=\frac{2}{9}\frac{R_P^2}{L^2} \tag{5}$$

where R_p is the particle radius (which implicitly indicates that we refer to spherical particles; for the sake of completeness it should also be noted that the alternate well-known definition of the Stokes number St_ξ, accounting for particle size and mass effect at the same time, may be recovered by multiplying St by ξ, i.e. $St_\xi= \xi St$).

These initial arguments clarify the concept that, for the phenomena of interest, vibrations can affect particle dynamics via two independent but concurrent mechanisms, i.e. the force which is produced by the time-periodic acceleration field as a results of the different density of the particles with respect to the surrounding fluid (a purely inertial effect) and the flow of thermovibrational nature that tends to transport particles in a more or less efficient way depending on their radius (in turn, as explained before, the latter consists of two contributions, i.e. the aforementioned 'mean' and 'instantaneous' velocity components). Obviously, another important parameter is the mass load, which (as explained in detail in Sect. 2.4) depends on the effective number of particles present in the fluid.

2.2 Hybrid Eulerian-Lagrangian formulation

A key observation regarding these problems is that experimental measurements aimed to get quantitative data are extremely difficult (almost impossible) in normal gravity conditions, given the disturbing presence of gravity (which would tend to demix particles from the fluid due to sedimentation of flotation). On the other hand, conducting tests in microgravity conditions is extremely expensive. In practice (while waiting for opportunities for space experiments, Lappa et al.,[66]), the most convenient way to gain an understanding of the underlying flow physics is to use numerical simulation. This explains why the existing literature on this subject relies to an unusual level on insights obtained via theoretical models and ensuing computations.

In such a context, however, the assumption of one-way coupled particle-fluid systems, which so much success has enjoyed in earlier works on the subject, should obviously be regarded as a non-viable option. For the specific problem considered here, the numerical treatment of these processes shall necessarily imply adequate physical and mathematical modeling of the mechanisms relating to the transfer of momentum from the particles to the surrounding fluid and vice versa. This naturally leads to the aforementioned concept of "two-way" coupling, by which the two considered (solid and liquid) phases can experience a 'mutual interference'.

In principle, many approaches could be applied to meet the objectives set at the beginning of Sect. 2. These strategies can be split into three main classes according to the nature of the model used to track the dispersed phase: capturing (also known as moving grid or Lagrangian approach, see Uchiyama[67]), Eulerian (also known as fixed-grid approach, see, e.g., Bothe et al., [68]) and combined 'hybrid' techniques (see e.g., Mark et al.,[69] for a review) by which special additional markers are tracked separately to reconstruct the interface between the different phases (see, e.g., Homma et al.,[70]) or the Eulerian governing equations in the fluid domain are 'extended' to the particle domain by constraining the motion inside the particles to a rigid motion (Haeri and Shrimpton[71]).

Following already successful attempts (Pushkin et al.,[24]; Melnikov et al.,[25]; Lappa[28-29, 56]), here, in particular, we resort to a hybrid formulation by which, while fluid flow is approached in the framework of a Eulerian description (leading to the classical Navier-Stokes equations valid for a continuum), the transport of particles is handled on the basis of a Lagrangian method that can account for each particle as a separate entity interacting with the 'environment'. The novelty of the present work with respect to earlier efforts (Lappa[56-59,64]) is obviously due to the two-way-coupled nature of the resulting approach, which (as we will illustrate in Sect. 2.3) requires proper physical reasoning and modifications or 'additional terms' to be considered for the Navier-Stokes equations.

2.3 Governing Equations

In order to develop further the ideas discussed above, in the present section, we lay the foundation of the overall numerical approach by transcending specific cases and introducing the fundamental equations that govern the considered dynamics. Anyhow, for the convenience of the reader, advanced formal discussions are limited to a minimum and the problem is described with a relatively simple formalism (making reference to preceding works when additional layers of knowledge are particularly appropriate).

The starting point for the fluid phase is obviously represented by the classical Navier-Stokes equations, which, for an incompressible fluid, can be cast in condensed form as

$$\underline{\nabla} \cdot \underline{V} = 0 \tag{6}$$

$$\rho \frac{\partial \underline{V}}{\partial t} = -\underline{\nabla} p - \rho \underline{\nabla} \cdot \left[\underline{V} \underline{V} \right] + \mu \nabla^2 \underline{V} + \rho \mathrm{b}\ \omega^2 \sin(\omega\ \mathrm{t}) \underline{\hat{n}} + \underline{S}_m \tag{7}$$

$$\rho C_v \frac{\partial T}{\partial t} + \rho C_v \underline{\nabla} \cdot \left[\underline{V} T \right] = \lambda \nabla^2 T \tag{8}$$

where the vector $\underline{V}$ contains the variables [u, v, w] (u, v and w being its velocity components along the x, y and z directions), p is the pressure, T is the temperature and ρ, μ, λ and C_v are the fluid density, dynamic viscosity, thermal conductivity and specific heat at constant volume, respectively. Moreover, the additional vector quantity $\underline{S}_m$ at the right-hand side of eq. (7) is the term required to properly couple the liquid and solid phases (notably, it makes the resulting approach formally similar to that implemented by Ref[72] to investigate the dynamics of shock waves traveling in a dusty gas, as we shall further detail in Sect. 2.4).

Using a Lagrangian approach, particles must obviously be considered as isolated, microscopic quantities compared with field variables. Nevertheless, the typical forces acting on them and the ensuing effects on particle motion can be taken into account solving the so-called Maxey-Riley equation. A short overview of this equation is given in the following, the reader being referred to Maxey and Riley[73] and Kuhlmann et al.,[74] for a more detailed discussion. In vector form this equation reads:

$$\rho_p \frac{d\underline{V}_p}{dt} = \rho \frac{D\underline{V}}{Dt} + \frac{9}{2} f(\mathrm{Re}_p) \frac{\mu}{R_p^2} \left(\underline{V} - \underline{V}_p \right) + \frac{\rho}{2} \left(\frac{D\underline{V}}{Dt} - \frac{d\underline{V}_p}{dt} \right) + \left(\rho_p - \rho \right) \mathrm{b}\ \omega^2 \sin(\omega\ \mathrm{t}) \underline{\hat{n}} \tag{9}$$

where $\underline{V}_p$ =[u_p, v_p, w_p] is the particle velocity and Re_p is the related instantaneous Reynolds number, defined as

$$\mathrm{Re}_p = \frac{2 R_p \rho \left| \underline{V} - \underline{V}_p \right|}{\mu} \tag{10a}$$

f(Re$_p$) is a corrective factor required to account for the departure of the drag from the classical Stokes law (Clift et al.,[75]):

$$f\left(\mathrm{Re}_p\right) = 1 + 0.15\, \mathrm{Re}_p^{\ 0.687} \tag{10b}$$

Notably, assembled in this way, equation (9) can be seen as a balance of forces. Indeed, the four contributions at its right-hand side represent, respectively, the force exerted on the generic particle by the undisturbed flow, the drag, the virtual-added mass force and the time-varying buoyancy force resulting from the application of vibrations. The so-called Basset force is neglected as the considered flow frequencies are within the limits that allow doing so (see Ref[30] and references therein for an extensive treatment of this aspect, which is not duplicated here for the sake of brevity).

The liquid velocity $\underline{V}$ appearing in this equation has to be 'reconstructed' at each particle location from the surrounding grid locations, which requires a proper interpolation scheme for problem closure (we will come back to this concept in Sect.3.1).

2.4 Two-way coupling aspects

The so-called "one-way" class of numerical methods[24-25, 28-29, 31, 56,74,76] relies on the assumption that the particle mass loading $\chi=\xi\varphi$ (ratio of the overall solid mass and liquid mass, where φ is the ratio of the volume globally occupied by the particles and the volume of the computational domain, i.e. the 'volume fraction') is so small that the influence of the dispersed phase on the liquid can be ignored. In such a context, one is therefore allowed to account for the effect of the local fluid-phase velocity on particle motion, whereas vice versa is not mandatorily required. If φ is relatively high (typically if $\varphi\geq10^{-6}$, Elgobashi[77]; see also Bodnar et al.,[78]), however, return effects must be properly taken into account, this being accomplished via the presence of the interphase coupling terms $\underline{S}$ in Eq. (7). In order to make the overall approach physically consistent, this term must obviously be determined for each control volume. This leads to the need for an algorithm able to identify the particles present at a given instant in any computational cell of the domain. Formally speaking, by denoting this number as n_{ijk} (*i, j* and *k* being the representative indexes of the *x, y* and *z* directions, respectively), the interphase term can be expressed (see, e.g., Eaton[79]; Bianco et al.,[80]) for each computational cell as

$$\left(\underline{S}_m\right)_{ijk} = -\frac{1}{\delta\Omega_{fluid}}\sum_{\ell=1}^{n_{ijk}} m_{p\ell}\frac{d\underline{V}_{p\ell}}{dt} \tag{11a}$$

$$\delta\Omega_{fluid} = \delta\Omega_{ijk} - n_{ijk}\frac{4}{3}\pi R_p^3 \tag{11b}$$

The sign minus in front of the summation simply indicates that an acceleration of particles ($\mathrm{d}\underline{V}_p/\mathrm{d}t>0$) is reflected in a corresponding deceleration of the thermovibrational flow ($\partial\underline{V}/\partial t<0$) and vice versa. The quantities m_p and $\delta\Omega_{ijk}$ are the mass of the generic particle and the volume of the computational cell containing it, namely, $m_p = \rho_p\frac{4}{3}\pi R_p^3$, $\delta\Omega_{ijk} = \Delta x\Delta y\Delta z$. Moreover, $\delta\Omega_{fluid}$ represents the amount of fluid contained in the computational cell. By simple geometrical considerations this quantity can formally be obtained by subtracting the volume of all particles located in the cell to $\delta\Omega_{ijk} = \Delta x\Delta y\Delta z$.

An important assumption underlying this modus operandi, however, is the condition that the volume of the generic particle is smaller than the volume of the computational cell, i.e. $\phi<1$ where $\phi = \frac{4}{3}\pi R_p^3 / \Delta x\Delta y\Delta z$. In practice, this is formally needed to justify that particles can be treated as microscopic quantities compared with the size of a typical mesh cell. Notably, this requirement may

also be regarded as a mathematical constraint for the maximum tolerable number of grid points used to discretize the problem, or alternatively for the maximum possible diameter of the particles for a given grid resolution (the interested reader being referred to Lappa et al.,[72] for additional elaboration of these concepts).

Another important quantity is the total number of particles. This number, obviously, is not arbitrary but depends on three distinct factors, namely, the considered mass loading χ and particle size and density. Such inter-dependences can be expressed mathematically as:

$$\chi = \frac{N_{part}\rho_p \frac{4}{3}\pi R_p^3}{\rho\Omega} \quad \rightarrow N_{part} = \frac{\chi}{\xi}\frac{\Omega}{\frac{4}{3}\pi R_p^3} \tag{12}$$

where Ω is the overall volume of the three-dimensional (3D) domain that is initially seeded with particles.

Other key observations concern the lack of coupling terms to be considered for eqs. (6) and (8), which also requires proper physical reasoning and justification.

An explanation for the absence of a mass coupling term can be elaborated in its simplest form on the basis of the argument that, while the liquid and the dispersed solid mass exchange momentum (indeed, most of the dynamics presented in this work stem from this effect), there is no corresponding mass exchange between these two phases (the overall mass of liquid and that of particles are conserved separately). To elucidate further the significance of this observation, one may consider that the mass of the present particles is fixed, i.e. they do not undergo any mass decrease or increase in time.

The corresponding justification for the energy equation is a little bit more elaborated. It requires introducing the global heat capacity of each phase as the product of its specific heat coefficient and mass and the *ratio* of these capacities for the solid and liquid phases:

$$H_c = \frac{C_{p(solid)}}{C_{p(liquid)}}\frac{N_{part}\rho_p \frac{4}{3}\pi R_p^3}{\rho\Omega} = \varepsilon\xi\varphi \qquad \text{where } \varepsilon = \frac{C_{p(solid)}}{C_{p(liquid)}} \quad \text{and } \varphi = \frac{\chi}{\xi} \tag{13}$$

For most of existing liquids the specific heat coefficient is almost one order of magnitude larger than the corresponding value for a solid, e.g., for water at 20 °C it is C_p=4186 $JKg^{-1}K^{-1}$ whereas for glass (the material used for the particles that will be used for the space experiments described in Ref[66]) it is 840 $JKg^{-1}K^{-1}$. Therefore, assuming $\varepsilon=O(10^{-1})$, $\xi=O(1)$ and $\varphi=O(10^{-2})$ (this being the worst case in terms of particle volume fraction φ, as further discussed in Sect. 2.5), it follows that $H_c=O(10^{-3})<<1$. The next step of this logical process consists of taking into account the link between the notion of heat capacity and that of *thermal inertia*. The latter is generally defined as the degree of slowness with which the temperature of the considered phase reaches that of the surroundings or, in an equivalent way, as *the capacity of the phase to store heat and to delay its transmission*. Given these premises, the simple estimates reported above lead to the straightforward

conclusion that in many circumstances the solid phase can be considered in *thermal equilibrium* with the liquid one (which alleviates the user form the burden of solving an extra Lagrangian equation for the transport of heat associated with particles and adding a corresponding interphase term to eq. (8)).

Another key point concerns the thermal expansion coefficient. This is assumed to be one order of magnitude smaller for the solid (e.g., β_T=2.07x10^{-4} and 0.255 x10^{-4} K^{-1}, yet at 20 °C, for water and glass, respectively), which explains why the dependence of the solid density on temperature is not taken into account in the present study.

2.5 Boussinesq approximation and Nondimensional formulation

In line with earlier efforts in the literature for the specific case of thermovibrational flow[50, 42], we assume as reference length, velocity and time, the cavity size (L), the thermal diffusion velocity (α/L) and time (L^2/α), respectively (where $\alpha=\lambda/\rho C_p$ is the fluid thermal diffusivity). Moreover, the temperature scaled by a reference values T_{ref}, is made non-dimensional as (T- T_{ref})/ΔT. With such choices and using the Boussinesq approximation to account for the dependence of the density on temperature (all the other liquid physical properties being considered constant), all the relevant Eulerian and Lagrangian equations involved in the present computational framework can finally be cast in non-dimensional form as

$$\underline{\nabla}\cdot\underline{V}=0 \tag{14}$$

$$\frac{\partial \underline{V}}{\partial t}=-\underline{\nabla}p-\underline{\nabla}\cdot\left[\underline{V}\underline{V}\right]+\mathrm{Pr}\,\nabla^2\underline{V}+\mathrm{Pr}\,Ra_{\omega}T\sin(\varpi t)\hat{\underline{n}}+\underline{S}_m \tag{15}$$

$$\frac{\partial T}{\partial t}+\underline{\nabla}\cdot\left[\underline{V}T\right]=\nabla^2 T \tag{16}$$

$$\frac{d\underline{V}_p}{dt}=\frac{1}{\xi+1/2}\left[-\frac{\mathrm{Pr}}{St}f(\mathrm{Re}_p)\left(\underline{V}_p-\underline{V}\right)+\frac{3}{2}\frac{d\underline{V}}{dt}+\frac{3}{2}\left(\underline{V}\cdot\underline{\nabla V}\right)\right]+\frac{\xi-1}{\xi+1/2}\gamma\sin(\varpi t)\hat{\underline{n}} \tag{17}$$

Equation (17) includes the viscous drag forces (first term at the right hand side) and the added mass effect relating to the material derivative of the fluid velocity (second and third terms).

Moreover, the following relationships hold:

$$\mathrm{Re}_p=3\sqrt{2}\frac{St^{1/2}}{\mathrm{Pr}}\left|\underline{V}_p-\underline{V}\right| \tag{18}$$

$$\chi=9\sqrt{2}\pi\frac{N_{part}\xi St^{3/2}}{\Omega^*}\rightarrow N_{part}=\frac{\Omega^*}{9\sqrt{2}\pi St^{3/2}}\frac{\chi}{\xi} \tag{19}$$

(Ω^* being the non-dimensional cavity volume Ω/L^3) and

$$\underline{S}_m = -\frac{1}{\delta\Omega^*_{ijk} - n_{ijk} 9\sqrt{2}\pi St^{3/2}} \sum_{\ell=1}^{n_{ijk}} 9\sqrt{2}\pi\xi St^{3/2} \frac{d\underline{V}_{p\ell}}{dt} \tag{20}$$

(where, for consistency, $\delta\Omega^*_{ijk} = \Delta x\Delta y\Delta z / L^3$).

A necessary pre-requisite for the applicability of this approach concerns the particle Stokes number, which must be very small, i.e. $St<<1$ (Kuhlmann et al.,[74]). Moreover, the following two additional inequalities must be satisfied:

$$\phi = \frac{9\sqrt{2}\pi St^{3/2}}{\Delta x^* \Delta y^* \Delta z^*} < 1 \tag{21}$$

$$\varphi = \frac{\chi}{\xi} = 9\sqrt{2}\pi \frac{N_{part} St^{3/2}}{\Omega^*} < O(10^{-2}) \tag{22}$$

where, as explained before, the first condition is equivalent to stating that particles are microscopic (ϕ being the ratio of the volume of a single particle and of the generic computational cell). In line with earlier works on the subject (Greifzu et al.,[81] and references therein), the second independent constraint (involving φ, i.e. the ratio of the volume globally taken by the particles and the volume of the entire computational domain) is needed to satisfy the assumption *that particle-to-particle interactions* (collisions, lubrication forces or other effects resulting from particle mutual interference, also known as four-way coupling) *can be neglected*. Although, strictly speaking, this inequality has been found to hold for isotropic turbulence and some authors have shown that constraints based on this type of flow can be overly conservative for simply time-periodic flows such as those considered in the present work (Capobianchi and Lappa[38]), we consider it as a limiting conditions for our model.

2.6 Initial and Boundary conditions

The governing equations must be complemented by the initial and boundary conditions required to close the problem from a mathematical point of view.

As initial conditions for the fluid we consider:

$$t=0: \quad \underline{V}(x,y,z) = 0, \; T(x,y,z) = z \tag{23}$$

where $\underline{V}=0$ implies $u=v=w=0$, i.e. the liquid is motionless with a linear temperature profile along the z coordinate (the temperature is $T_{Cold} = 0$ on the cold sidewall and $T_{Hot} = 1$ on the other side).

Moreover, at t=0, particles are distributed uniformly and with zero velocity.

The boundary conditions for t>0 consist of the classical no-slip constraint on all the walls, i.e.

$u=v=w=0$ on $\partial\Omega$ (24)

Isothermal conditions at z=0 and z=1.

$T=0$ for z=0 (25a)

$T=1$ for z=1 (25b)

and adiabatic conditions for the other walls.
For what concerns the particles, in line with earlier studies[56,57], these are assumed to interact in a non-elastic fashion with walls, i.e. they can approach the solid boundary until at a distance not smaller than their radius is achieved; thereafter, they are allowed to slide along the boundary until the wall-normal velocity component changes sign (allowing the particles to leave the wall).

3. The Numerical Method

After building an appropriate mathematical representation of the considered system, the next step obviously relates to the selection of an adequate numerical procedure to solve the underlying equations.

3.1 The Projection method

As solution technique we have implemented a projection method based on the use of primitive variables (namely, velocity, pressure and temperature). The mathematical prerequisite at the basis of this class of methods has its origin in the so-called decomposition theorem for vector fields (the so-called Hodge theorem, see, e.g., Ladyzhenskaya[82]). According to this theorem, a general vector field can always be decomposed into a part of given divergence and the gradient of a scalar potential function; thereby, the mathematical problem relating to the need to determine a velocity field that satisfies the continuity equation and develops vorticity (as required by the viscous nature of the fluid) can be articulated in a numerical procedure where these two aspects are formally taken into account *separately* (in practice, this process is mediated by the relationship between the pressure and the velocity fields as further illustrated below).
Initially, a simplified momentum equation where pressure is neglected is solved:

$$\frac{\partial \underline{V}^*}{\partial t} = \left[-\underline{\nabla} \cdot \left(\underline{V}\underline{V} \right) + \mathrm{Pr} \ \ \nabla^2 \underline{V} + \mathrm{Pr}\, \nabla^2 \underline{V} + \mathrm{Pr}\, Ra_\omega T \sin(\varpi t) \hat{\underline{n}} + \underline{S}_m \right]^n \tag{26}$$

where the superscript 'n' indicates the time step. Obviously, this leads to a velocity field that has no physical meaning (nevertheless, from a purely mathematical point of view, it possesses the correct amount of vorticity as the pressure gradient does not directly contribute to the curl of the velocity field, i.e. $\underline{\nabla} \wedge \underline{V}$).

As second stage, an additional elliptic equation resulting from the substitution of the velocity field $\underline{V}^{n+1}$ into the continuity equation is integrated:

$$\nabla^2 p = \frac{1}{\Delta t} \underline{\nabla} \cdot \underline{V}^* \tag{27}$$

and the intermediate (non-physical) velocity field is corrected using the resulting pressure to account for the conservation of mass:

$$\underline{V}^{n+1} = \underline{V}^* - \Delta t \underline{\nabla} p \tag{28}$$

Such a two-step procedure provides a velocity field that is solenoidal ($\underline{\nabla} \cdot \underline{V} = 0$). Moreover since $\underline{\nabla} \wedge \underline{V}^{n+1} = \underline{\nabla} \wedge \underline{V}^*$, this flow has also the *correct content of vorticity* as required by the original version of the momentum balance equation (Eq. 15). Given the theoretical implications of the "inverse theorem of calculus", the resulting field can be considered *unique* from a mathematical point of view and *consistent* from a physical standpoint (the interested reader being also referred, e.g., to Shen[83]; Armfield and Street[84]; Lee et al.,[85]; Guermond et al.,[86]).

As indicated by eqs. (26)-(28), we have implemented this numerical technique using schemes explicit in time. In particular, given the extremely small velocities involved in the present problems, the convective and diffusive terms appearing in both the momentum and the energy equations have been discretized with standard central differences. In order to improve the coupling between pressure and velocity (see, e.g., Choi et al.,[87-88]), however, a staggered arrangement has been used for these two quantities, that is, while the components of velocity *u, v* and *w* occupy the center of the cell face perpendicular to the x, y and z axes, respectively (see, e.g., Refs[89-90]), pressure is located in the center of each computational cell.

The particle tracking equation re-arranged to have $d\underline{V}_p/dt$ appearing only at the left-hand side (as made evident by eq. (17)) has been integrated with an explicit in time 4th order Runge-Kutta scheme. The fluid velocity at the generic particle location, needed for the integration of this equation has been determined at each time step starting from nodal values on the staggered grid and resorting to simple linear interpolation[64]. As similar approach (linear interpolation relying on the available values at the points of the fixed Eulerian grid) has been used for the material derivative $D\underline{V}/Dt$ (required for evaluating the force exerted by the undisturbed flow on the particle and the virtual-added mass force). Put simply, the nodal values taken by this quantity determined as

$$\frac{\underline{V}^{n}-\underline{V}^{n-1}}{\Delta t}+\left[\underline{\nabla}\cdot\left(\underline{V}\underline{V}\right)\right]^{n} \tag{29}$$

have been stored at each time step in a dedicated array, in order to be used for the derivation of $D\underline{V}/Dt$ at the particle position via linear interpolation.

For all the simulations, the time integration step has been kept smaller than St/Pr in order to resolve properly the particle relaxation time. Moreover, a grid refinement study has been carried out to ensure grid-independence. In line with the mesh refinement study conducted by Ref[50], a resolution corresponding to 80 grid points along each spatial direction has been found to be more than sufficient (this finding reflects the known fortunate absence of boundary layers in thermovibrational flow for the range of values of the Gershuni number considered in the present work).

3.2 Validation:

Given the nature of the problem addressed in the present study, finding relevant results produced by other authors to be used for validation purposes was not straightforward as one would imagine. For this reason, after unsuccessfully sifting through plenty of existing studies available in the literature with different (non relevant) foci, we decided to validate the overall theoretical architecture illustrated in Sects. 2.1-2.6 and 3.1 through comparison with the outputs of simulations conducted using a *different computational platform* (for the same circumstances considered in the present work). As independent software, in particular, we have considered ANSYS Fluent given the availability of a reliable two-way coupled approach for particle tracking directly coded into this package.

For incompressible flow, ANSYS Fluent is based on a primitive-variable method pertaining to the same category of projection techniques described in Sect. 3.1, namely, the so-called SIMPLE (Semi-implicit Method for Pressure Linked Equations) method (see Patankar[91]). In place of the staggered arrangement of variables (described in Sect. 3.1), however, this software is dependent on a collocated grid approach, which means that all the physical quantities of interest are defined in the center of the grid cells. For this reason, (in order to resolve properly the physical coupling of velocity and pressure), ANSYS Fluent relies on the special interpolation schemes by Rhie e Chow[92]. We have used this package to solve the classical set of balance equations for mass, momentum and energy reported in Sect. 2.3 using 2nd order upwind schemes for all convective terms (standard central differences have been employed for the diffusive terms only). With ANSYS Fluent all these terms are typically handled *implicitly* (with the sole exception of the buoyancy contribution, the only entity being treated explicitly). Moreover, in order to accelerate convergence, this software takes advantage of a classical Algebraic Multigrid scheme (AMG) with standard parameters (the so-called Gauss-Seidel smoother, see, e.g., Hutchinson and Raithby[93].

A dedicated discussion is also needed for the particle motion equation. Fluent integrates it in its original formulation (eq. (9)) with a 5th order Runge-Kutta scheme (Cash and Karp[94]). While the

particle velocity appearing in the drag contribution is treated in an implicit way, all the other terms are dealt with explicitly (which might be regarded as another difference with respect to the implementation described in Sect. 3.1, where all terms present in both the Navier-Stokes and the Maxey-Riley equations were handled in the framework of a time-explicit scheme).

For what concerns the evaluation of the forces acting on particles, we have selected the following options available in Fluent: the "barycentric method" to reconstruct the fluid velocity at the instantaneous positions occupied by particles (needed to evaluate the drag), and bi-linear interpolation and first order Euler schemes to determine the material derivative $D\underline{V}/Dt$ (needed to account for the force exerted by the undisturbed flow on the particle and the virtual-added mass force).

The accuracy control implemented naturally by Fluent allows the use of different time steps for the particle motion equation and the Navier-Stokes equations. By setting the accuracy control to 10^{-5} we have enforced an integration time step lower than the relaxation time of the particles. With such settings, in particular, particles have been forced to perform 'at least' 3 steps in a cell for every time step relating to the integration of the Navier-Stokes equations.

Results produced with Fluent are reported in Fig. 2 where they are directly compared with the equivalent ones yielded by the computational platform described in Sect. 2 and 3.1. The reader is directly referred to the figure caption for detailed information about the representative cases for which simulations conducted with the two platforms have been compared.

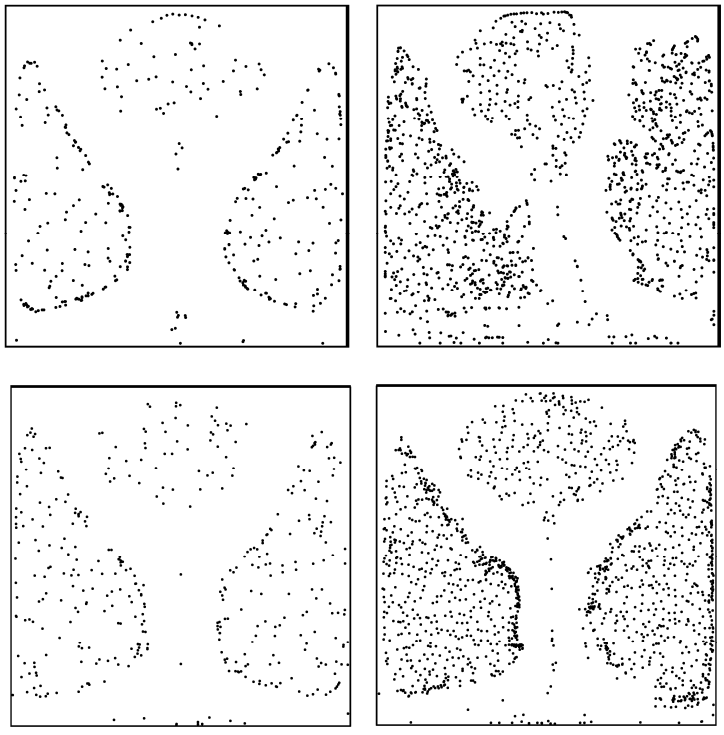

(a), t≅10

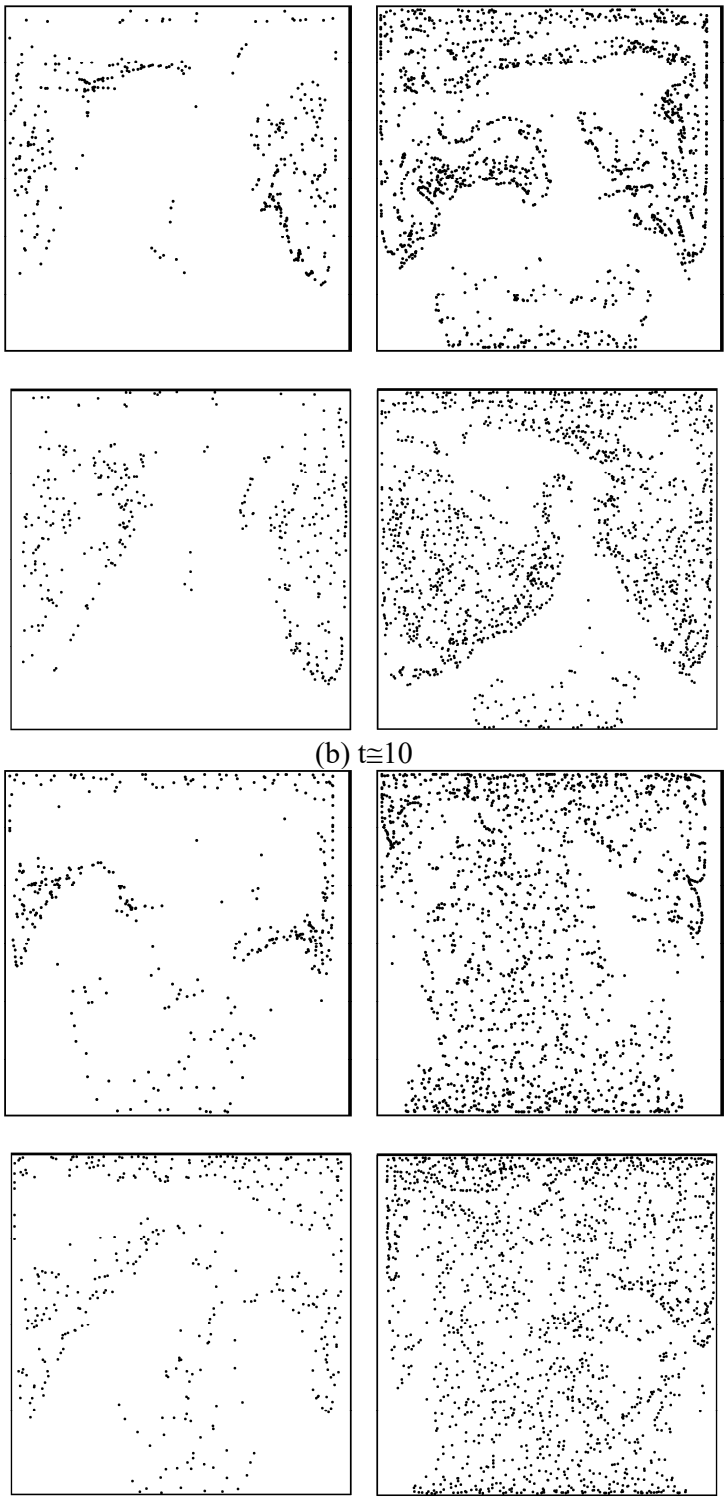

(b) t≅10

(c) t≅5

Figure 2: Comparison of numerical results (two-way coupling) obtained with the present computational platform and ANSYS Fluent for Pr=6.11, St=5x10^{-6}, Ra_{ω}= 10^5 and different values of ξ, γ and ϖ. For each case, four snapshots are shown; in particular, the left and right frames relate to two different values of the particle volume fraction (namely, φ=3.6x10^{-3} and φ=2.8x10^{-2}), while the top and bottom frames represent results obtained with the present platform and ANSYS Fluent, respectively: a) ξ=0.5, γ=1x10^8, ϖ=5x10^3; b) ξ=2.0, γ=1x10^8, ϖ=5x10^3; c) ξ=1.5, γ=5x10^8, ϖ=10^4.

All simulations have been initialized with a uniform distribution of particles. The minor visible differences between the present and the Fluent-based results should be ascribed to the slightly different initial positions considered for particles and/or to the fact that the snapshots do not relate exactly to the same times (due to the different time integration steps required by the two platforms) and/or to the different interpolation schemes used by Fluent and the present code. The very good agreement made evident by these figures (despite the significant differences in the underlying numerical strategies) should be regarded as a good indicator of the lack of implementation errors and the physical relevance of the findings. As a concluding remark for this section, we wish to highlight that other comparisons demonstrating consistency were also considered for the 3D cases (not shown).

4. Results

As already explained to a certain extent in the introduction, the present work stems from the argument that a dense distribution of solid particles in a fluid undergoing thermovibrational convection may disturb the underlying transport mechanisms, thereby setting an upper limit (in terms of parameter φ for fixed particle size and density) to the effective formation of ordered particle structures.

In this section the potential of the proposed new framework is demonstrated by considering a series of representative cases of practical complexity and relevance (i.e. suitable for the definition of real experiments to be conducted in space) and the ensuing results are presented following a specific order, which reflects the need to implement a precise analysis hierarchy. In particular, two important intertwined issues are addressed, i.e. the concurrent possibilities to influence the particle-forming mechanisms by increasing the density of particles or their overall amount, i.e. the volume fraction (both leading to an increase in the mass load).

As we will illustrate in the remainder of this section, vibrated particle-fluid systems can be extremely sensitive to these parameters and produce spontaneous 'asymmetries'. Resolving these questions therefore also requires estimating *the role played by the dimensionality of the problem* (that is the number of space dimensions involved). This is the reason why some of the explorative simulations are also conducted in a two-dimensional (2D) framework (we will come back to this important concept later).

Pattern formation in these processes is described here with respect to particle motion, related structures, and the convective multicellular patterns arising as a consequence of vibrational buoyancy forces. The following values or ranges of the characteristic parameters (defined in Sect. 2) are considered: Prandtl number (Pr=6.11 corresponding to pure water at ambient temperature), non-dimensional vibration angular frequency $10^3 \leq \varpi \leq 10^4$, Rayleigh number $10^4 \leq Ra_\omega \leq 10^5$, non-dimensional acceleration amplitude $10^8 \leq \gamma \leq 5\text{x}10^8$, density ratio $0.1 \leq \xi \leq 2$and $St=5\text{x}10^{-6}$ (all these non-dimensional parameters reflect the space hardware and materials described in Ref[66], namely cubic fluid containers with size L= 1cm, ΔT in the range 0.5 – 15 °C, vibrations with frequency

spanning the interval 1 – 2.8 Hz, acceleration amplitude between 2.8 and 9.6 m/s^2 and particles made of glass, with various densities and diameter ≅90 μm). Though, for consistency with the companion study conducted by Lappa and Burel[64], the Stokes number is fixed to St=5x10^{-6}, the volume fraction of particles is allowed to span a relatively wide interval, which combined with the considered set of values of ξ, leads to a wide range of mass loads (χ). We wish also to recall that, as illustrated by Refs[56,57], if the density of the particles is set equal to the density of the liquid, no particle attractors exist. Particles would remain uniformly distributed in the fluid, which explains why the case ξ=1 is not considered.

4.1 The quadrupolar field

Continuing in a similar vein to Ref[64], most conveniently, we start from a short description of the so-called time-averaged flow, i.e. the convective effects that are produced in addition to the instantaneous ones when the Gershuni number takes relatively high values and vibrations are perpendicular to the imposed temperature gradient.

In ideal conditions, that is, with no particles being dispersed in the fluid that can disturb it (see Fig. 3), this type of convection typically gives rise in rectangular cavities to the so-called *quadrupolar field*, i.e. a set of four rolls satisfying conditions of symmetry with respect to the horizontal and vertical axes. Such symmetry can be broken if the direction of vibrations is not perpendicular to the imposed temperature gradient and/or if the Gershuni number exceeds a given threshold. In such conditions, the original perfectly centro-symmetric distribution of rolls is taken over by a single roll pervasive throughout the physical domain with two small counter-rotating cells located in opposing corners of the cavity (Khalloufet al.,[95]; Lappa[96]; Lappa and Burel[64]).

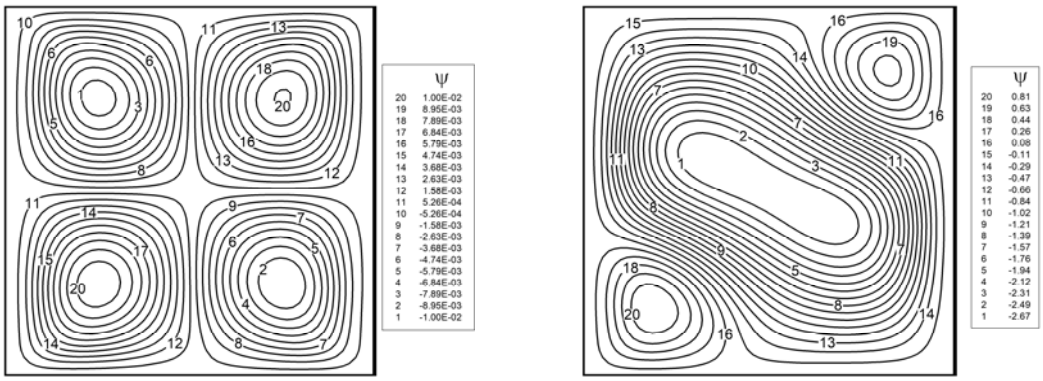

a) b)

Figure 3: Typical time-averaged flow in thermovibrational convection (water, 2D computations): a) Ra_ω=10^5, ϖ=10^4 → Gs= 305 (quadrupolar field), b) Ra_ω=10^6, ϖ=10^4 → Gs=3.05x10^4 (single roll field).

Apart from displaying a quadrupolar pattern, the time-averaged flow for relatively small values of *Gs*, is also steady and relatively *weak*. This means that if, at the same time, the Rayleigh number (eq. (2)) is high, *the oscillatory components of the velocity field are dominant* [as implicit in eq. (3), for high Ra_ω, conditions of small *Gs* can be attained if the angular frequency of the vibrations is sufficiently large].

In particular, as illustrated by Ref[56], the dominant instantaneous flow (for a square enclosure, small *Gs* and high Ra_ω) simply consists of a single roll occupying the entire cavity, which continuously changes its sense of rotation (from the clockwise to the counter-clockwise orientation) in a *consistent way* with respect to the direction of the time-varying acceleration.

Without particles, indeed, the flow response to the applied vibrations is, in general, perfectly synchronous, that is, if the forcing has non-dimensional frequency ϖ, the signal measured by a generic probe put in the fluid in terms of instantaneous velocity or temperature will display exactly the same frequency (and/or frequencies that are multiples of ϖ, i.e. higher order harmonics). The signal will obviously also include a time-averaged component, which, as explained before, can take negligible or appreciable values depending on the specific regime considered. As shown, e.g., by Savino and Lappa[42], the detectable steady component in the signal is close to zero if ϖ is relatively small (in such conditions the flow is dominated by the instantaneous component of velocity). As stated before, however, the relative importance of the time-averaged flow can be weakened also for high ϖ provided *Gs* is sufficiently small (i.e. Ra_ω is large). As anticipated in Sect. 2.1, while the amplitude of the instantaneous velocity grows with Ra_ω, the magnitude of its time-averaged parts increases with *Gs*[56].

Since the interplay between the non-symmetric pattern shown in Fig. 3b and the emerging particle structures has been already examined in a companion work[64], in the present study we will limit ourselves to considering values of $Gs \leq O(10^3)$ for which the time-averaged flow is weak and it always corresponds to the classical quadrupolar pattern depicted in Fig. 3a.

4.2 Fluid and particles under the effect of vibrations

The preliminary descriptions elaborated in Sect. 4.1 (dealing only with purely fluid-dynamic aspects) logically pave the way to the present section, where particles are added to the fluid. As the main criterion to judge on the ability of two-way coupled particles to influence the overall system dynamics, in particular, we consider the perturbations that they can create in the flow spatio-temporal behavior. As a testbed for such analysis (without loss of generality), we consider again the classical two-dimensional square cavity (Figs. 4-10).

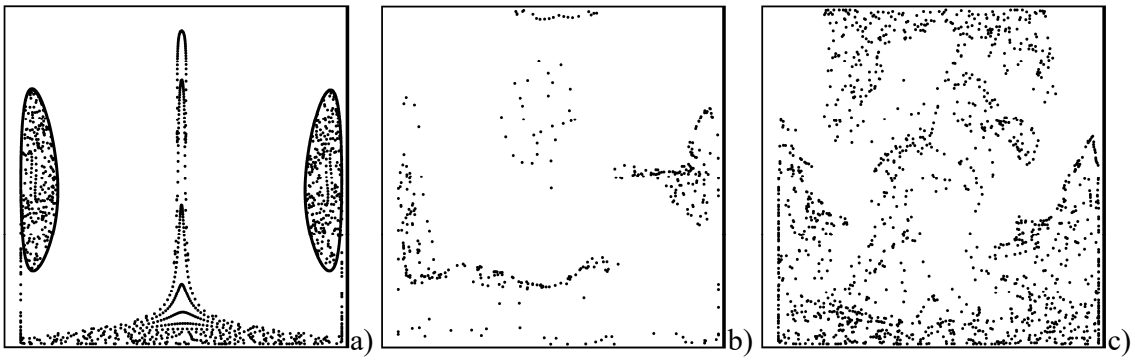

Figure 4: Snapshots of particle distribution (2D computations) for $\gamma=5\text{x}10^{8}$, $Ra_{\omega}=10^{5}$, $\varpi=10^{4}$ (Gs=305) and $\xi=0.5$ at $t\cong5$: a) one-way coupling, b) two-way coupling and $\varphi=3.6\text{x}10^{-3}$, c) two-way coupling and $\varphi=2.8\text{x}10^{-2}$.

As an example, Fig. 4 shows the outcomes of the numerical simulations carried out neglecting the back influence of particles on fluid flow (see, e.g., Fig. 4a for $\xi=0.5$) together with equivalent computations conducted in the frame of the two-way coupling model (Figs. 4b). As outlined above, this extension to 1-way coupled results is intentionally used to verify by cross-comparison the efficacy of particles in disturbing the carrier thermovibrational flow. In such a context, indeed, it is worth recalling that with the one-way coupled approach inertial particles are 'merely' transported, i.e. their number has no impact on the characteristics of the carrier flow (a high number of particles being used only to reveal the perfection of the underlying attractors which behave as 'templates' for their accumulation, Fig. 4a). Along the same lines, we also allow (see Fig. 4c) the volume fraction φ to exceed the limit for which a four-way coupling approach would be required. This 'license' (which we take only for the 2D results, as all the 3D results presented in the remainder of this study obviously obey the constraint $\varphi<O(10^{-2})$) is intentionally used to determine in a simplified framework the conditions in which, even by filtering out the disturbing particle-to-particle effects, the back influence of particles on fluid flow would be so large to eventually prevent the manifestation of the sought attractors.

Given these premises, some initial insights follow naturally from a comparison of Figs. 4a and 4b. While Fig. 4a shows the classical two accumulation loops already extensively reported in previous studies (the flow being insensitive to the amount of particles[56-59]), in Fig. 4b, it can be seen that for particle volume fraction $\varphi=3.6\text{x}10^{-3}$, the perfect symmetry and high-resolution appearance of the structures is taken over by a less ordered distribution. Though the existence of attracting regions is still recognizable, a series of 'disturbances' can be detected. These disturbances manifest themselves in the form of 'eruptions' of swarms of particles occasionally leaving the (left and right) accumulation regions (visible in Fig. 4b as horizontal jets, i.e. distribution of particles elongated in the direction of the applied vibrations).

Notably, by changing φ there are an uncountable number of such patterns, which differ in the degree of disorder. This is the reason why, to elucidate further the impact of this parameter, we have increased it by one order of magnitude (the limiting case with $\varphi=2.8\text{x}10^{-2}$ shown in Fig. 4c). This

figure is useful as it reveals that, even if particle interaction and related effects are neglected, *a too high mass load* can definitely prevent particles from being accumulated. This is equivalent to stating that an upper boundary in terms of φ (or χ) must be put on the region of existence of attractors potentially identifiable in the frame of one-way coupling models. In other words, this means that the 'attractee' can effectively manifest in the form of well-recognizable structures of particles only if χ does not exceed a certain threshold value.

Following up on the previous point, as a fruitful alternative for obtaining additional insights into these behaviors we have examined the velocity signals measured by a numerical probe located in a representative point (the geometrical center of the cavity). These are shown in Fig. 5.

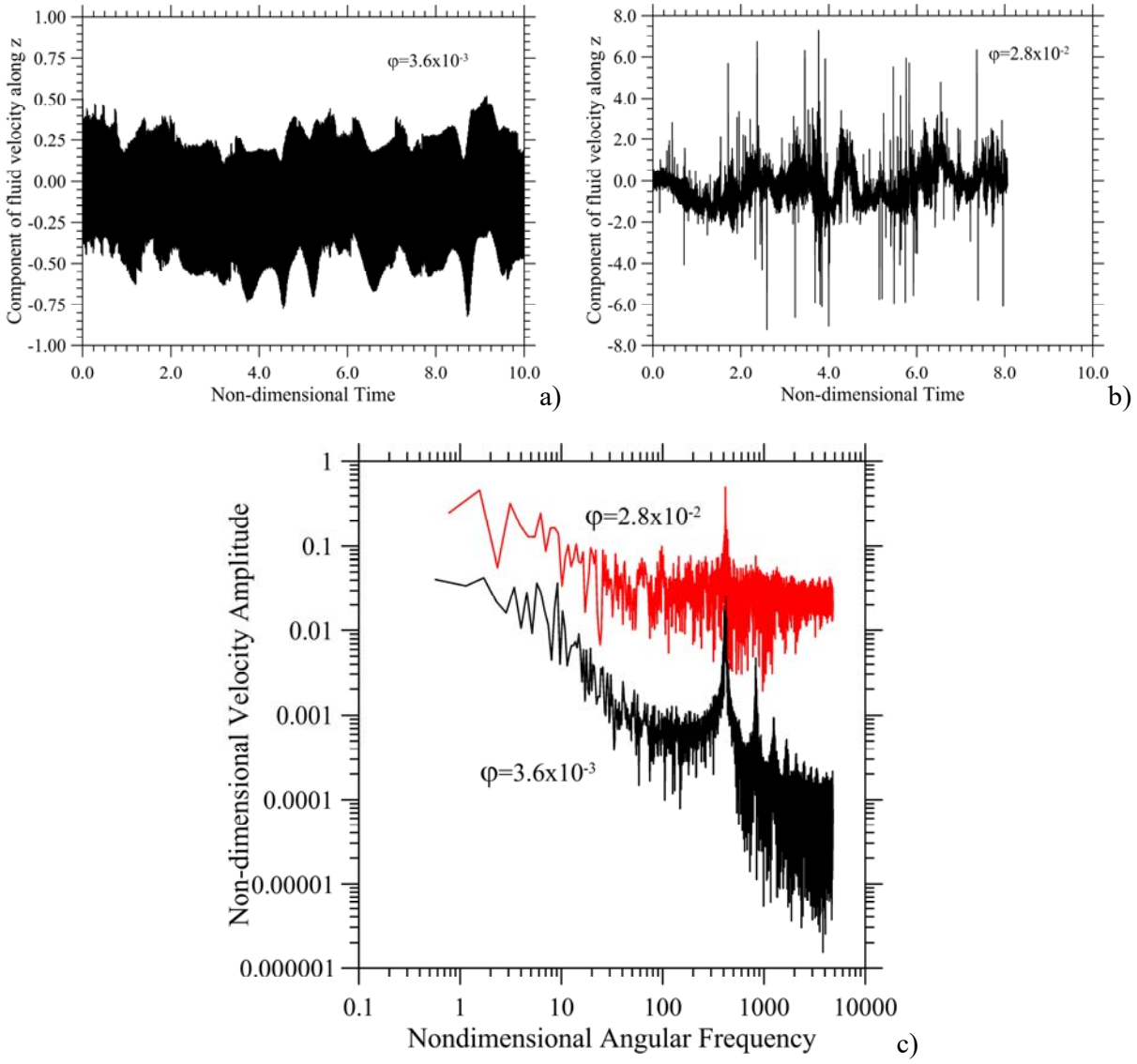

Figure 5: Fluid velocity component along the z direction in the center of the cavity as a function of time (2D computations, two-way coupling) for $\gamma=5\times10^{8}$, $Ra_{\omega}=10^{5}$, $\varpi=10^{4}$ (Gs=305) and ξ=0.5: a) $\varphi=3.6\times10^{-3}$, b) $\varphi=2.8\times10^{-2}$;c) frequency spectra for the signals shown in panels (a) and (b).

This figure is instrumental in demonstrating that the back influence of particles on the fluid can make the resulting flow *essentially non-periodic*. Indeed, a series of long period disturbances can be recognized in Fig. 5a while Fig. 5b displays a much more complex frequency spectrum.

These plots can also be used for another interesting interpretation. Figure 5c (containing the frequency spectra related to the signals shown in Figs. 5a and 5b), indeed, demonstrates that the average amplitude of the velocity signal can significantly be increased for a fixed value ξ on making φ larger. We can readily see the physical significance of this finding by reflecting on the transfer of momentum between solid particles and fluid. Under the effect of vibrations, particles can gain momentum directly as a result of the induced acceleration and their different density with respect to the surrounding liquid. Part of this momentum is transferred (via viscous effects, i.e. particle drag) from particles to fluid, thereby *energizing the fluid flow*.

Put simply, the presence of particles plays the role of an extra source of momentum for the fluid (formally represented by $\underline{S}_{\mathrm{m}}$ in eq. (15)) in addition to the classical buoyancy term ($\mathrm{Pr}\, Ra_{\omega} T \sin(\varpi t)\underline{\hat{n}}$). This feedback mechanism can therefore be seen as the root cause for the increase in the amplitude of the signal visible in Fig. 5b (corresponding to the red line in Fig. 5c), the manifestation of which (in terms of patterning behavior) is the *recognizable strong asymmetry in the distribution of particles* (Fig. 4c).

Another meaningful way to think about the back influence of particles is to consider the effect they can exert on the fluid from a time-averaged standpoint. This aspect is quantitatively and qualitatively substantiated by Fig. 6 for $\varphi=3.6\text{x}10^{-3}$.

Though the classical four cells typical of the quadrupolar field can somehow still be identified, their morphology is highly distorted. Moreover, topological defects such as cracks, cusps and discontinuities start to affect the streamlines. They witness directly the ability of particles to exchange momentum with the fluid; in Fig. 6 it can also be seen that the quadrupolar field for the considered value of *Gs* is no longer time-independent, i.e. it changes with time.

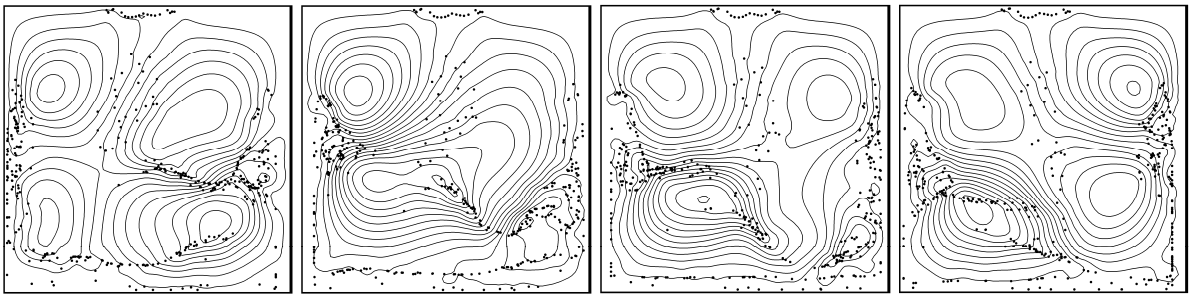

Figure 6: Time-averaged fluid velocity field for $\gamma=5\text{x}10^{8}$, $Ra_{\omega}=10^{5}$, $\varpi=10^{4}$ (*Gs*=305), $\xi=0.5$ and $\varphi=3.6\text{x}10^{-3}$ (2D computations, two-way coupling, four snapshots evenly spaced in time, Δtime = 0.25, $\psi_{\min}=-0.08$, $\psi_{\max}=0.08$) .

Another related key observation concerns the strength of the time-averaged convection, which tends to be higher when particles are present ($\psi_{\max}=8\text{x}10^{-2}$ in place of $\psi_{\max}=1\text{x}10^{-2}$ without particles).

This provides additional independent confirmation that *on average* there *is a net transfer of momentum from particles to the fluid*.

The situation dramatically changes when φ is increased by one order of magnitude ($\varphi=2.8\text{x}10^{-2}$ in Fig. 7). The quadrupolar field is longer recognizable. The time-averaged convection is characterized by the continuous nucleation of cells that with time coalesce or split resulting in a more or less chaotic behavior (Fig. 7).

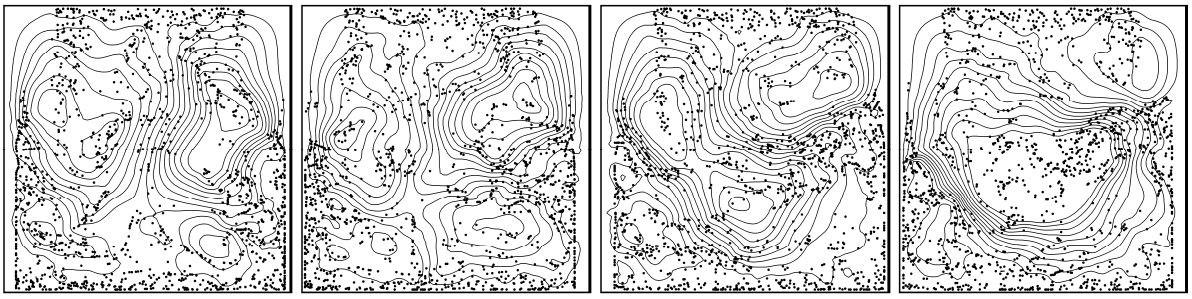

Figure 7: Time-averaged fluid velocity field for $\gamma=5\text{x}10^{8}$, $Ra_{\omega}=10^{5}$, $\varpi=10^{4}$ (Gs=305), $\xi=0.5$ and $\varphi=2.8\text{x}10^{-2}$ (2D computations, two-way coupling, four snapshots evenly spaced in time, Δtime = 0.25, $\psi_{min}=-0.2$, $\psi_{max}=0.2$) .

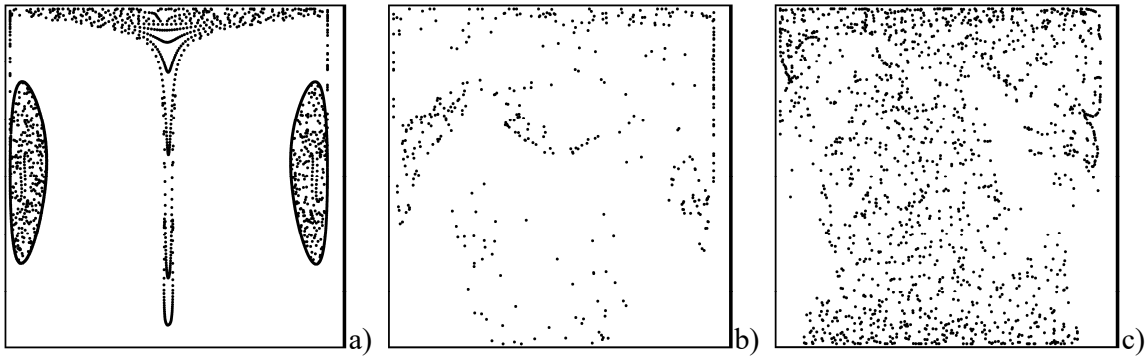

Figure 8: Snapshots of particle distribution (2D computations) for $\gamma=5\text{x}10^{8}$, $Ra_{\omega}=10^{5}$, $\varpi=10^{4}$ (Gs=305) and $\xi=1.5$ at t≅5: a) one-way coupling, b) two-way coupling and $\varphi=3.6\text{x}10^{-3}$, c) two-way coupling and $\varphi=2.8\text{x}10^{-2}$.

Continuing with the description of the numerical results, Fig. 8 may be regarded as the analog of Fig. 4 for a value of the density ratio larger than one ($\xi=1.5$), i.e. for particles denser than the fluid. Direct comparison with the situation where $\xi=0.5$ indicates that the disturbing effect exerted by particles for a fixed value of the particle volume fraction φ can be enhanced by increasing the density ratio. This obvious finding simply reflects the corresponding increase in the mass load $\chi=\varphi\xi$. Along these lines, what is emphasized in Fig. 9 is still the inter-relatedness of the disorder detectable in the particle distribution and the velocity signals and related frequency spectrum.

By taking a look at the vertical axes, the reader will easily realize that the fluid motion is yet energized by the interplay with the dispersed solid mass. The frequency spectrum, however, is more

involved, which indicates that the disturbances preventing the flow from taking a regular behavior are more complex and intense (compare the red lines in Figs. 9c and 5c). This trend is further confirmed by the patterns reported in Figs. 10 and 11 for $\varphi=3.6\text{x}10^{-3}$ and $\varphi=2.8\text{x}10^{-2}$, respectively.

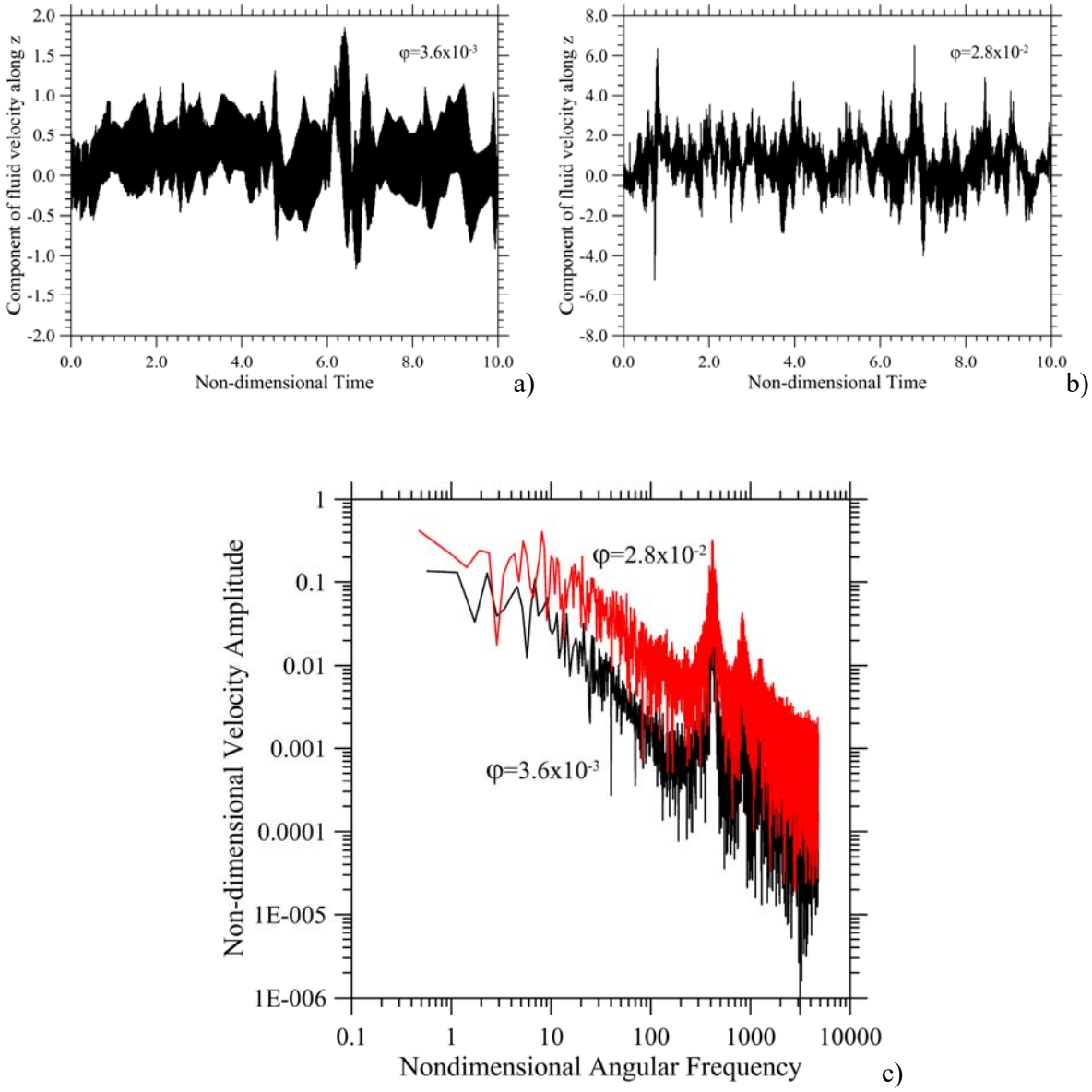

Figure 9: Fluid velocity component along the z direction in the center of the cavity as a function of time (2D computations, two-way coupling) for $\gamma=5\text{x}10^{8}$, $Ra_{\omega}=10^{5}$, $\varpi=10^{4}$ (Gs=305) and ξ=1.5: a) $\varphi=3.6\text{x}10^{-3}$ and b) $\varphi=2.8\text{x}10^{-2}$;c) frequency spectra for the signals shown in panels (a) and (b)

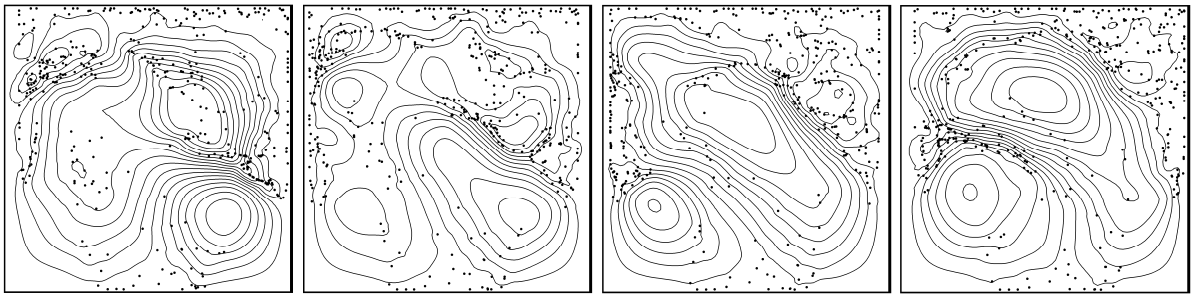

Figure 10: Time-averaged fluid velocity field for $\gamma=5\text{x}10^{8}$, $Ra_{\omega}=10^{5}$, $\varpi=10^{4}$ (Gs=305), ξ=1.5 and $\varphi=3.6\text{x}10^{-3}$ (2D computations, two-way coupling, four snapshots evenly spaced in time, Δtime = 0.25, ψ_{min}=-0.15, ψ_{max}=0.15).

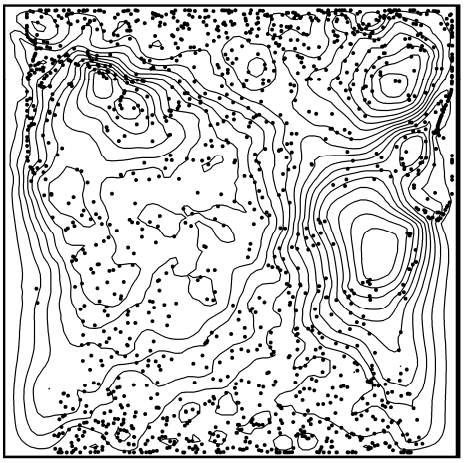

Figure 11: Snapshot of time-averaged fluid velocity field for $\gamma=5\text{x}10^{8}$, $Ra_{\omega}=10^{5}$, $\varpi=10^{4}$ (Gs=305), ξ=1.5 and $\varphi=2.8\text{x}10^{-2}$ (ψ_{min}=-0.25, ψ_{max}=0.25).

4.3 Symmetry breaking and three-dimensional effects

The simplification to two dimensions at the basis of all the results presented in the preceding two sections may seem natural at first sight because of the intrinsic symmetries of the system sketched in Fig. 1. Nevertheless, it should expressly be pointed out that, since the two-way coupled evolution of a non-isothermal fluid and dispersed solid particles under the effect of vibrations has not been investigated until now[56-59], there is no reason to think a priori that this interplay should not hide completely unknown mechanisms somehow involving the spanwise direction. This is the reason why we have intentionally based the present work on an analysis hierarchy implemented through a characteristic path of progression from 2D to 3D simulations. First two-dimensional simulations have been executed (where any processes that depend on the details of the third direction are excluded, Sect. 4.2), then, three-dimensional simulations have been conducted (present section) to reveal heretofore unseen 3D effects via intentional cross-comparison with the equivalent 2D ones.
Following the same approach undertaken in Sect. 4.2, in particular, in this section, first we discuss cases for which particles are lighter than the external fluid and then we focus on situations with ξ>1.

Along these lines, the outcomes of the 3D simulations for the same circumstances already considered in Fig. 4b are reported in Figs. 12 (3D snapshot of particle distribution) and Fig. 13 (related time evolution).

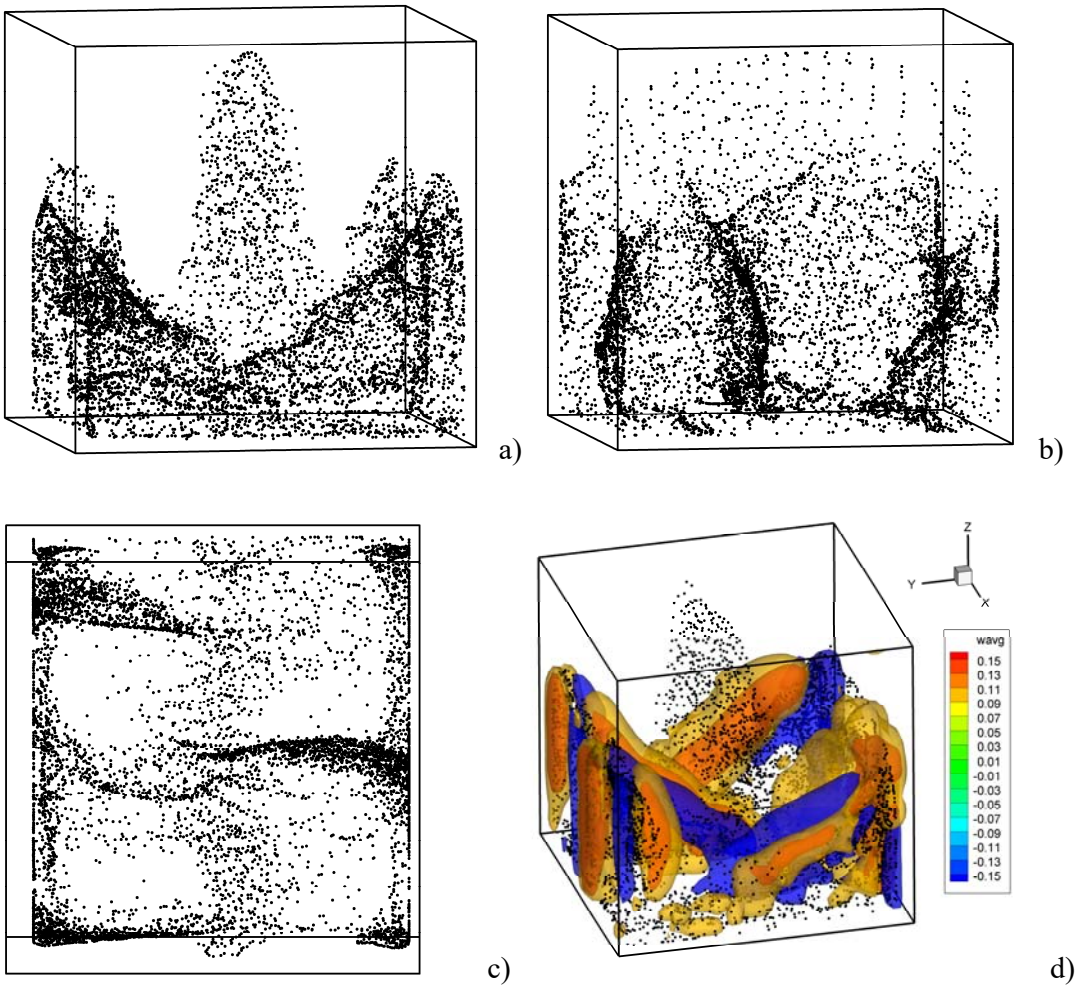

Figure 12: Snapshot (3D views for t≅5) of particle structures for $\gamma=5\text{x}10^{8}$, $Ra_{\omega}=10^{5}$, $\varpi=10^{4}$ (Gs=305), ξ=0.5 and $\varphi=3.6\text{x}10^{-3}$: a) perspective perpendicular to the yz plane, b) perspective perpendicular to the xz plane, c) perspective perpendicular to the xy plane, d) combined 3D view showing particles and isosurfaces of the fluid velocity component in the spanwise direction.

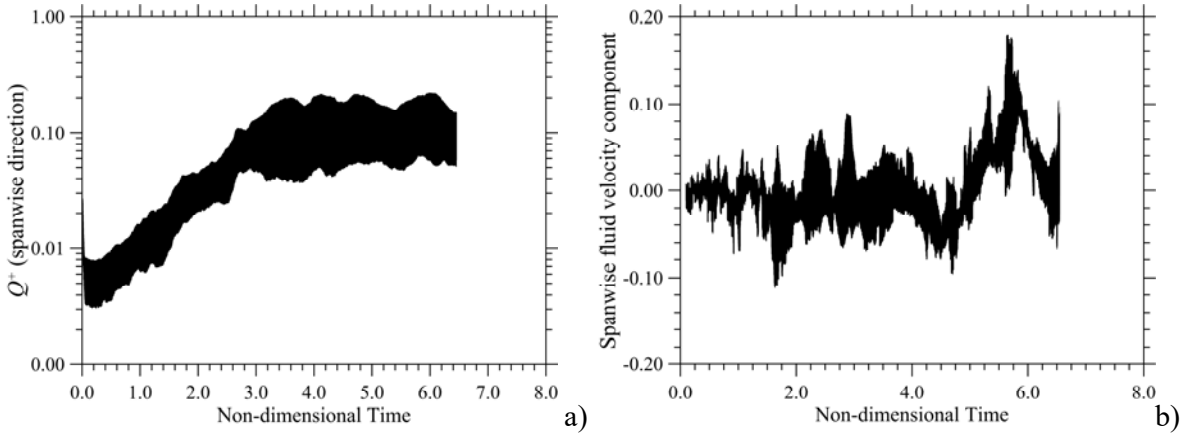

Figure 13: Evolution in time of 3D effects for γ=5x10^8, Ra_ω=10^5, ϖ=10^4 (Gs=305), ξ=0.5 and φ=3.6x10^{-3}: a) parameter Q^+, b) Fluid velocity component in the spanwise direction probed in the center of the cubic cavity.

As a fleeting glimpse into Fig. 12 would confirm, symmetry breaking phenomena with respect to the spanwise direction can effectively occur when particles have an additional spatial degree of freedom (i.e. they can move freely along x). This behavior becomes very evident if the distribution of particles is inspected by taking a look at it along an axis perpendicular to the xz (Fig. 12b) and xy (Fig. 12c) planes, respectively. Particles do not remain uniformly distributed along x (as the assumption of 2D behavior would require); rather they display some preferred planes of accumulation. More specifically, three disjoint main planes supporting clustering dynamics can be distinguished in Fig. 12b and 12c, one approximately located at the center of the cubic enclosure and two located in proximity to the walls delimiting it along the x direction.

The 3D self-organization of the particles also implies remarkable changes in the pattern that can be seen considering the projection of the solid mass distribution in the yz plane (compare e.g. Fig. 12a with Fig. 4b). Particles do still tend to cluster forming structures that an external observer (looking at the fluid domain along the x axis) would recognize. However, the morphology of these aggregates is quite different; the areas where solid matter is concentrated have an irregular triangular shape (in place of the elongated elliptical accumulation regions visible in Fig. 4b).

To put these results in a broader perspective, in the following we will attempt an interpretation of such variations in the morphology of the particle structures on the basis of the 'bifurcation theory'. Indeed, it is widely recognized in fluid-dynamics (and more in general in the field of non-linear systems) that the loss of symmetry implies the existence of a new solution that bifurcates from a pre-existing one due to the selection and ensuing amplification of disturbances (in this regard the solution shown in Fig. 4b could be regarded as the 'basic 2D state' from which the 3D state shown in Fig. 12 originates as time increases).

Although the analogy with the classical concept of bifurcation in fluid dynamics should effectively be considered as a possible key for the interpretation of these results, the identification of the related physical 'disturbances', that is, the cause-and-effect mechanisms responsible for the symmetry

breaking process, however, is not straightforward as one would assume. Since for the considered value of the Gershuni number no 3D instability occurs in pure thermovibrational flow (i.e. when no particles are considered) or when the back influence of the dispersed solid matter on the carrier flow is not taken into account (one-way coupling), we argue that its mechanism implicitly relies on the two-way coupling between fluid flow and particle motion, that is, the *3D disturbances take their energy from such an interplay*.

Interestingly, this may be regarded as another typical example of systems where separated entities can produce collective behaviors more complex than those of the individual components (see, e.g., Lappa and Ferialdi[97]). As revealed by the present 3D simulations, two-way coupled particles can provide these vibrated dispersions with the required internal feedback loops by which they can develop their own capacity for transformation, requiring only the right conditions for activation. As already described to a certain extent in Sect. 4.2, these processes (able to feed information back into the system where it is iterated, or used multiplicatively), are established in terms of *momentum exchange*.

The continuous exchange of momentum between fluid and particles enabled by particle drag and inertial effects can make these processes extremely sensitive to their (even though very small) internal variations allowing the amplification of initially extremely small disturbances. A clear separation should therefore be considered between these results and those previously obtained in the frame of the one-way approach by Lappa and Burel[64], where the observed 3D phenomena were essentially a consequence of the three-dimensional nature of the time-averaged field established inside the cavity for relatively high values of the Gershuni number (Gs=O(10^4)).

A snapshot of the numerically computed disturbances for the present case (that we represent in terms of the time-averaged fluid velocity component along the spanwise direction) can be seen in Fig. 12d. The highly-localized nature of these fluid-dynamic perturbations further supports our interpretation about the role played by the exchange of momentum between fluid and particles in inducing the 3D instability (indeed, the regions of the physical space where the fluid velocity spanwise component is significant *closely mimic* the distribution of particles).

The related temporal evolution is shown in Fig. 13. There the growth of 3D disturbances as time increases is presented in terms of the quantitative global measure already used by Ref[98] to account for the global displacement of particles transported by thermal plumes of gravitational nature

$$Q^{+} = \frac{\sum_{u_{part}>0} m_{part} u_{part}}{M_{tot}}, \quad Q^{-} = \frac{\sum_{u_{part}<0} m_{part} u_{part}}{M_{tot}} \tag{30}$$

where u_{part} is the velocity taken by particles along the x direction. From a practical standpoint, the quantity $Q^{\pm}$ may be seen as the instantaneous positive or negative momentum possessed by all particles along the spanwise direction, normalized by the total solid mass. It should not be confused

with the quantity plotted in Fig. 13b, which instead represents the (Eulerian) velocity *of the fluid* in the center of the cavity.

Further pursuing the possible analogy with the typical mechanisms of amplification of disturbances envisaged by the linear stability analysis (where the growth of perturbations is assumed to follow an exponential law, see, e.g., Ref[96]), Q^+ has been reported in Fig. 13a using a logarithmic scale. As the reader will easily realize, using such a scale the perturbations indeed grow following an apparently linear law, which confirms the exponential behavior of the disturbance growth process. This figure is useful as it also shows that after an initial transient time, disturbances saturate their amplitude and a new stable state is attained, which is consistent with the theory of bifurcations.

To do justice to these interesting findings, the next section is entirely devoted to a characterization of this bifurcation and identification of the conditions that make it possible.

4.4 The role of inertial effects

Starting from the arguments elaborated in the preceding section about the essentially inertial nature of the instability producing transition to 3D flow, the next natural step towards a complete characterization of this phenomenon would require proper assessment of the sensitivity of the symmetry breaking process to typical problem parameters, especially those that can exert an immediate impact on the momentum exchange between the two phases (namely the particle volume fraction (φ) , the acceleration amplitude (γ), the density ratio (ξ), and the Rayleigh number (Ra_ω)).

As shown in Fig. 14a, a decrease in the volume fraction of dispersed solid mass for a fixed value of ξ can change the time required for disturbance saturation, which provides additional important clues regarding the essentially inertial nature of the instability.

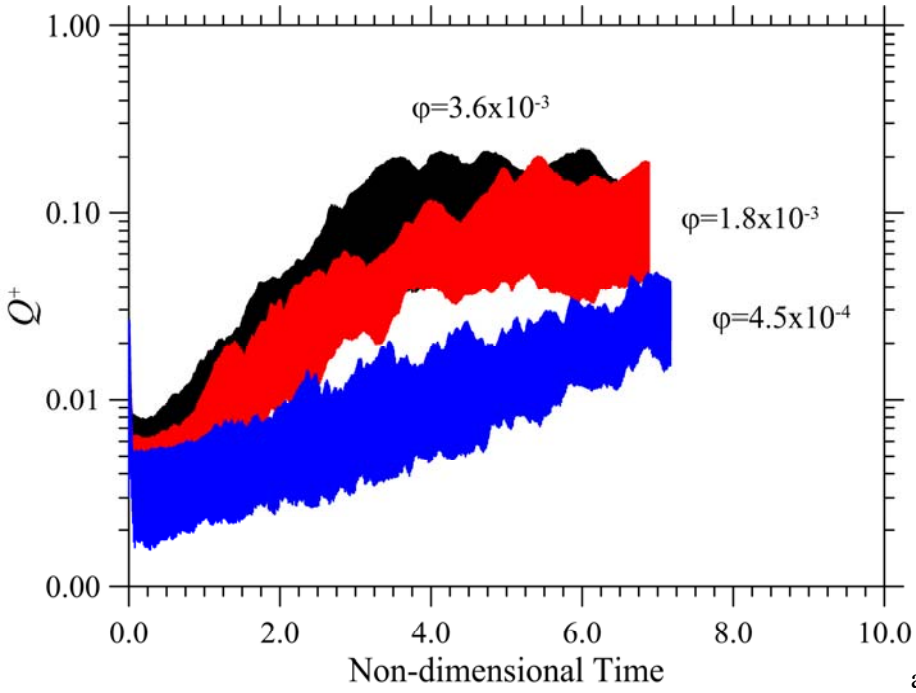

a)

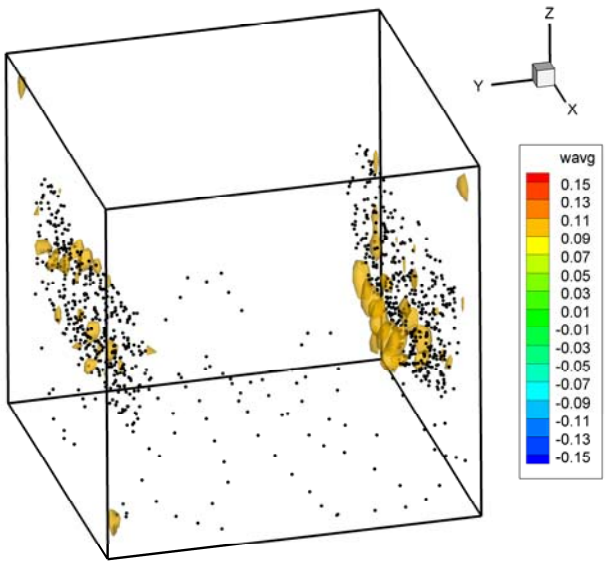

b)

Figure 14: (a) Evolution in time of the Q^+ parameter for $\gamma=5\text{x}10^8$, $Ra_\omega=10^5$, $\varpi=10^4$ (Gs=305), $\xi=0.5$ and three different values of the particle volume fraction φ, (b) Combined 3D view showing particles and isosurfaces of the fluid velocity component in the spanwise direction for $\varphi=4.5\text{x}10^{-4}$ and $t\cong5$.

Most interestingly, making φ smaller can even lead to conditions for which the emerging structure recovers the perfect geometrical morphology of the underlying attractors determined in the framework of 1-way coupled numerical studies (Fig. 14b to be compared with Fig. 8a). This figure also quantitatively substantiates the scarce role played in this case by the time-averaged fluid velocity component in the spanwise direction (it being limited in strength and present only in very localized regions).

Notably, similar effects can be obtained by properly tuning the acceleration amplitude. In this regard, Fig. 15 is extremely instructive as it proves that other situations exist for which the 3D disturbances are not excited and the pattern can retain its essentially two-dimensional configuration. These figures refer to the same value of the density ratio and particle volume fraction already considered for Fig. 12 ($\xi=0.5$ and $\varphi=3.6\text{x}10^{-3}$), i.e. the same mass load ($\chi=\varphi\xi$), but a *smaller values of* γ *and* ϖ ($\gamma=1\text{x}10^8$, $\varpi=5\text{x}10^3$).

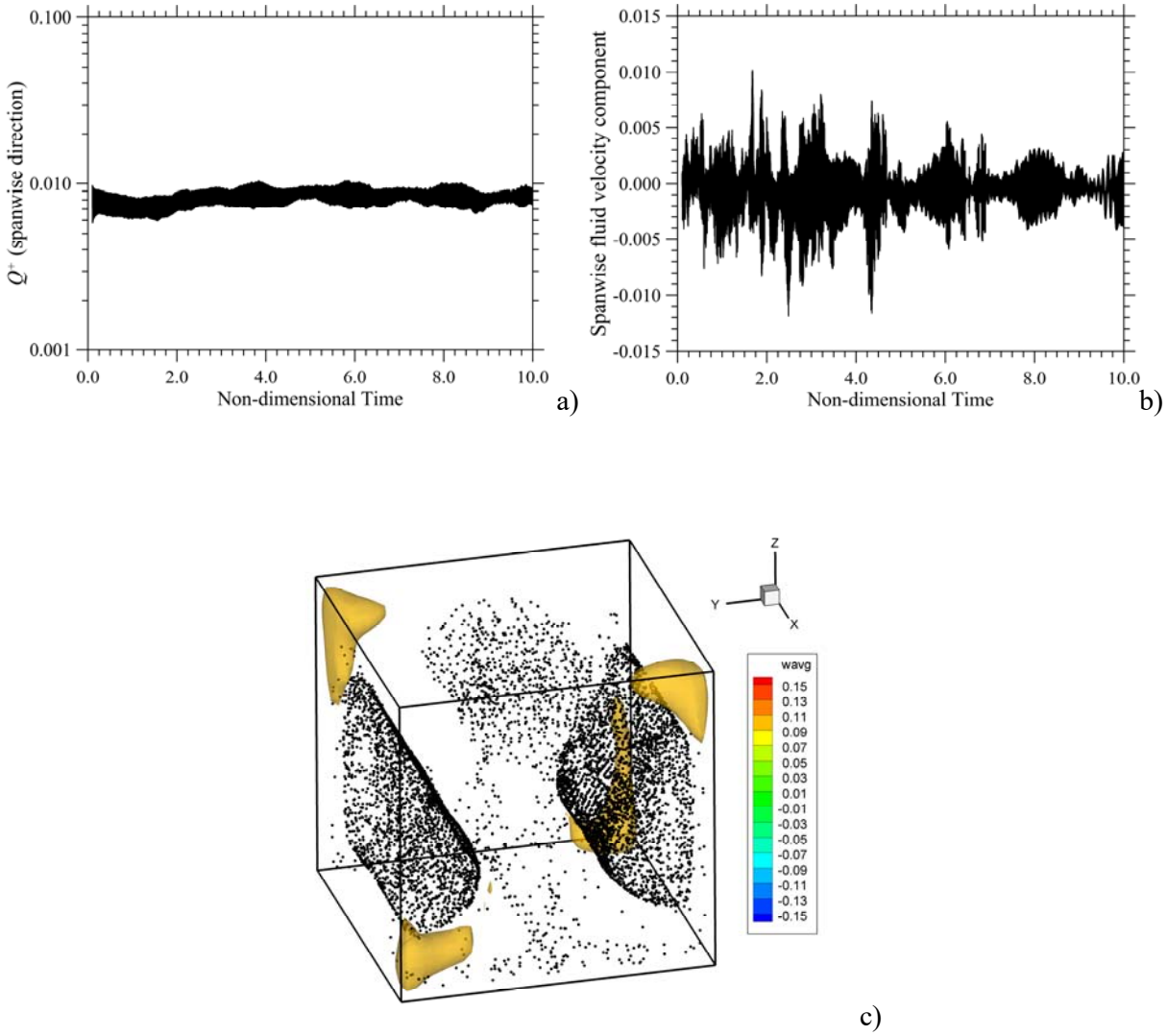

Figure 15: Evolution in time of 3D effects for $\gamma=1x10^8$, $Ra_\omega=10^5$, $\varpi=5x10^3$ (Gs=1220), $\xi=0.5$ and $\varphi=3.6x10^{-3}$: a) parameter Q^+, b) fluid velocity component in the spanwise direction probed in the center of the cubic cavity, c) combined 3D view showing particles and isosurfaces of the fluid velocity component in the spanwise direction for $t\cong10$.

We did not detect any symmetry breaking process for such conditions (the reader being directly referred to Fig. 15a and 15b for evidence of the essentially 2D behavior, witnessed by the order of magnitude of Q^+ and of the fluid velocity in the center of the cavity, respectively). Though a 3D disturbance exists (Fig. 15a), its amplitude and magnitude are relatively limited ($O(10^{-2})$); moreover, it displays no tendency to be amplified as time increases even if the simulation is prolonged up to 10 times the thermally diffusive reference time (for a cubic cavity having a size of 1 cm, this would correspond to a physical time of approximately two hours).

Along these lines, further understanding of the specific equilibrium conditions attained in this case can be gained by considering again simulations conducted under the constraint of two-dimensional flow (Figs. 16-18).

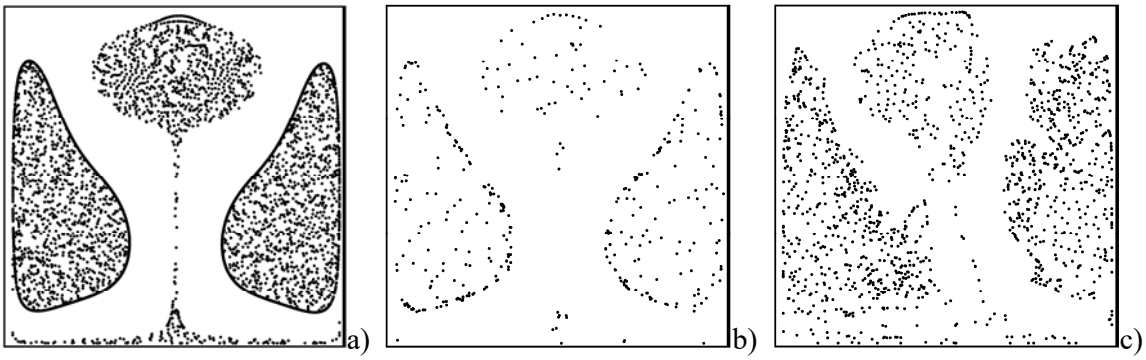

Figure 16: Snapshots of particle distribution (2D computations) for $\gamma=1x10^{8}$, $Ra_{\omega}=10^{5}$, $\varpi=5x10^{3}$ (Gs=1220) and $\xi=0.5$ at t≅10: a) one-way coupling, b) two-way coupling and $\varphi=3.6x10^{-3}$, c) two-way coupling and $\varphi=2.8x10^{-2}$.

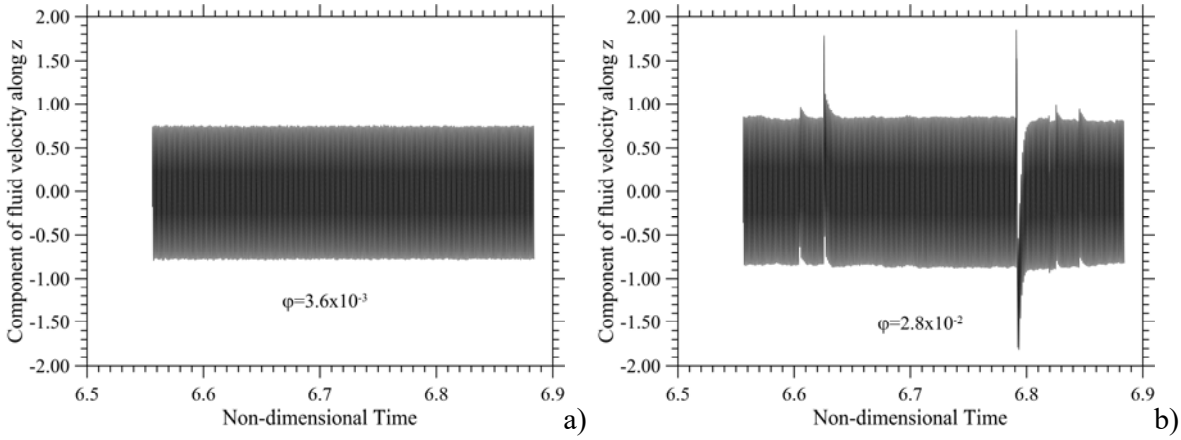

Figure 17: Fluid velocity component along the z direction in the center of the cavity as a function of time (2D computations, two-way coupling) for $\gamma=1x10^{8}$, $Ra_{\omega}=10^{5}$, $\varpi=5x10^{3}$ (Gs=1220) and $\xi=0.5$: a) $\varphi=3.6x10^{-3}$ and b) $\varphi=2.8x10^{-2}$.

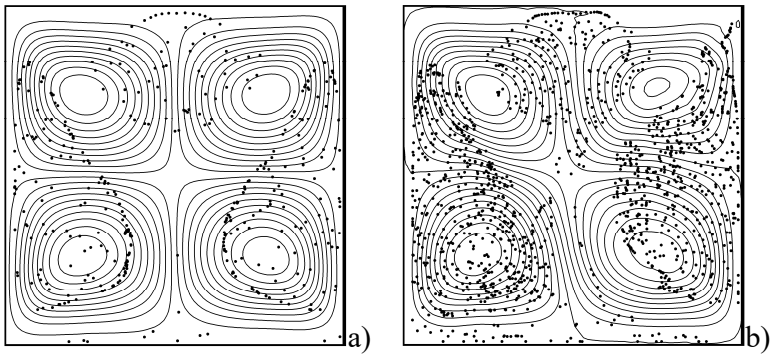

Figure 18: Single snapshot of time-averaged fluid velocity field for $\gamma=1x10^{8}$, $Ra_{\omega}=10^{5}$, $\varpi=5x10^{3}$ (Gs=1220), $\xi=0.5$: a) $\varphi=3.6x10^{-3}$ (ψ_{min}=-0.045, ψ_{max}=0.045), b) $\varphi=2.8x10^{-2}$ (ψ_{min}=-0.05, ψ_{max}=0.05).

These results are meaningful as they can be used yet to easily get quantitative information on the inertial mechanisms at work in the considered process. As a quick look at Fig. 17a would immediately confirm, the response of the fluid-particle mixture to the applied forcing is very regular for $\varphi=3.6\text{x}10^{-3}$. For the limiting condition represented by $\varphi=2.8\text{x}10^{-2}$, though some spikes can occasionally be seen in the signal, the behavior is still essentially time-periodic (Fig. 17b). The conceptual ingredient needed to understand these results lies in considering the impact of the parameter γ on particle acceleration (via eq. (17)) and on the associated momentum exchange term at the right hand side of the Navier-Stokes equations (represented by eq. (20)). By causing a decrease in the momentum transferred between the two phases, a decrease in γ is beneficial in terms of stability behavior because it limits the disturbances that particles can induce in the underlying fluid flow. Similar concepts also apply to the time-averaged field. The quadrupolar field visible in Fig. 18a can clearly be recognized even if the particle volume fraction is largely increased (Fig. 18b). These observations align with the trend visible in terms of patterning behavior in Fig. 16.

By limiting the energy that the system can use for the amplification of disturbances, a decrease in γ can make the overall system stable, this argument being fully supported by the 3D simulations (Fig. 15c).

There is also another interesting extension that attaches to this interpretation. An increase in ξ should, indeed, exert an opposite influence on the dynamics, i.e. it should promote the onset and growth of disturbances for a fixed value of γ (that is why in the reminder of this section we also probe the role of this factor). As an example, the outcomes of the 2D simulations for $\text{Ra}= 10^5$, $\gamma=1\text{x}10^8$, $\varpi=5\text{x}10^3$ and $\xi=2$ are summarized in Figs. 19-20.

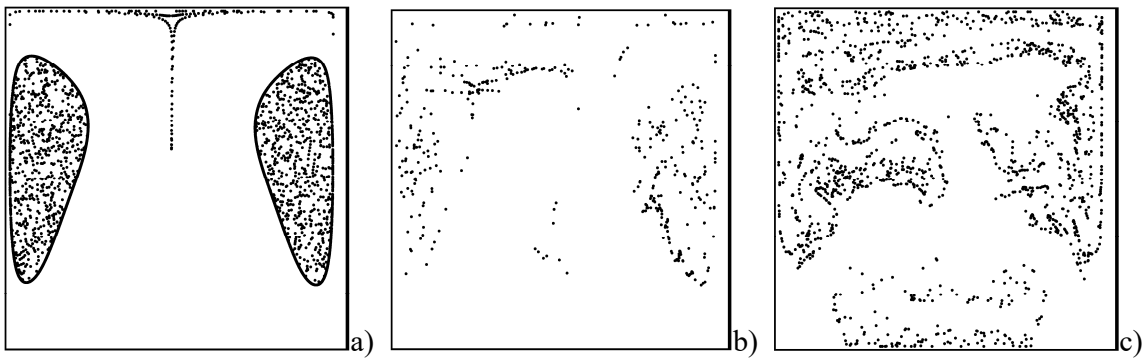

Figure 19: Snapshots of particle distribution (2D computations) for $\gamma=1\text{x}10^8$, $Ra_\omega=10^5$, $\varpi=5\text{x}10^3$ (Gs=1220) and $\xi=2$ at $t\cong10$: a) one-way coupling, b) two-way coupling and $\varphi=3.6\text{x}10^{-3}$, c) two-way coupling and $\varphi=2.8\text{x}10^{-2}$.

As evident in these figures, for the same value of the acceleration amplitude, vibration frequency, Rayleigh number, and particle volume fraction ($\varphi=3.6\text{x}10^{-3}$), but a higher value of ξ (corresponding to four times the mass load relating to Fig. 16b), the feedback loop by which disturbances can be excited starts to be effective. This is consistent with the presence of jets of particles being erupted from the structures in Fig. 19b and by the alterations undergone by the classical quadrupolar field

(see Fig. 20, interestingly, in these circumstances, the back influence of particles on fluid flow causes quite regular periodic coalescence and separation of time-averaged rolls located in opposing corners).

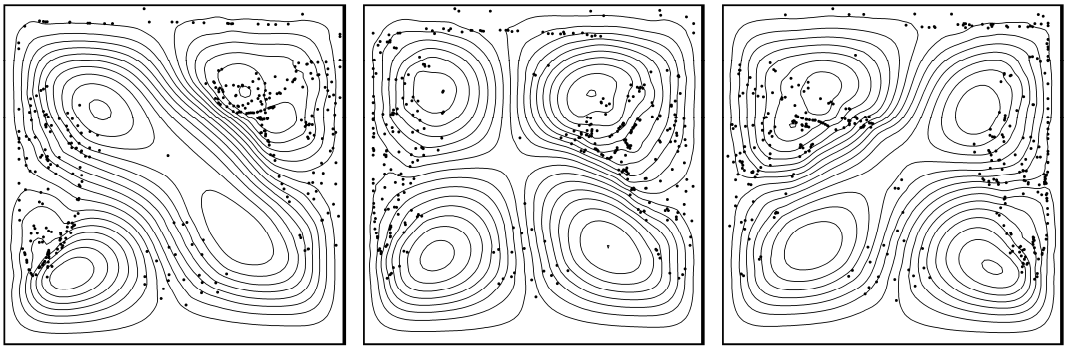

Figure 20: Time-averaged fluid velocity field for $\gamma=1\text{x}10^{8}$, $Ra_{\omega}=10^{5}$, $\varpi=5\text{x}10^{3}$ (Gs=1220), $\xi=2$ and $\varphi=3.6\text{x}10^{-3}$ (2D computations, two-way coupling, three snapshots evenly spaced in time, Δtime = 0.5, ψ_{min}=-0.075, ψ_{max}=0.075) .

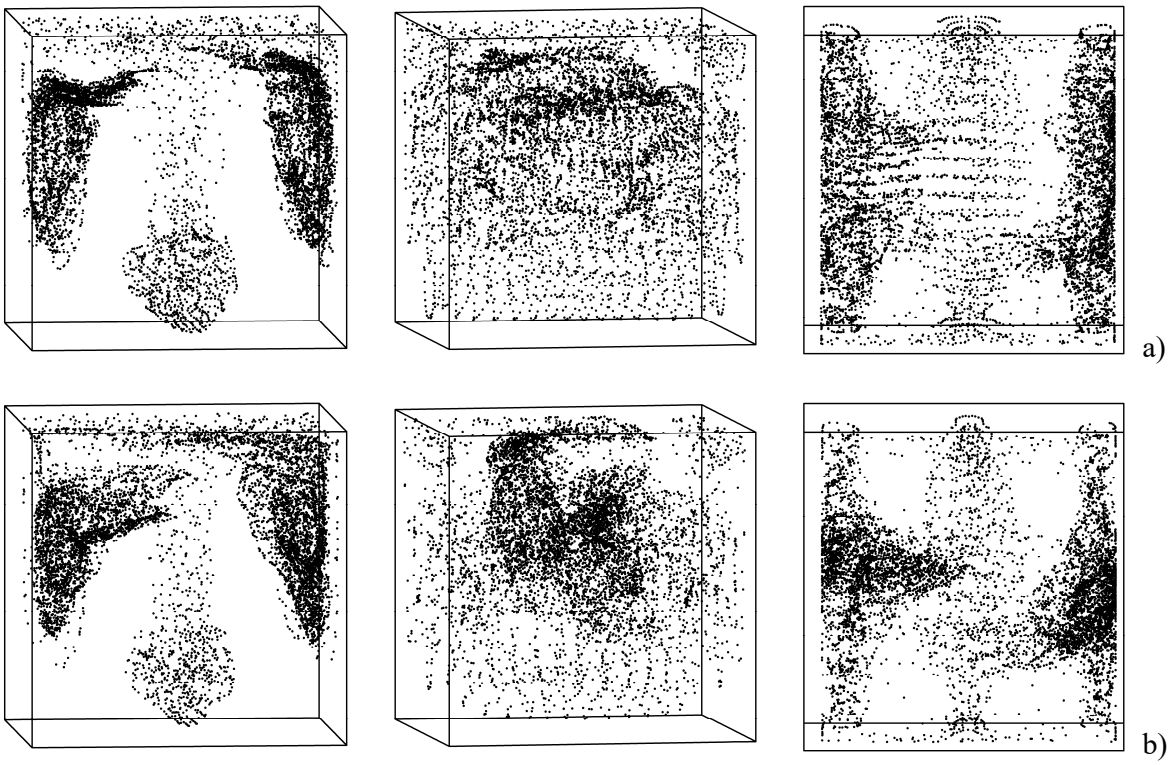

Fig. 21 – continued (see next page for figure caption)

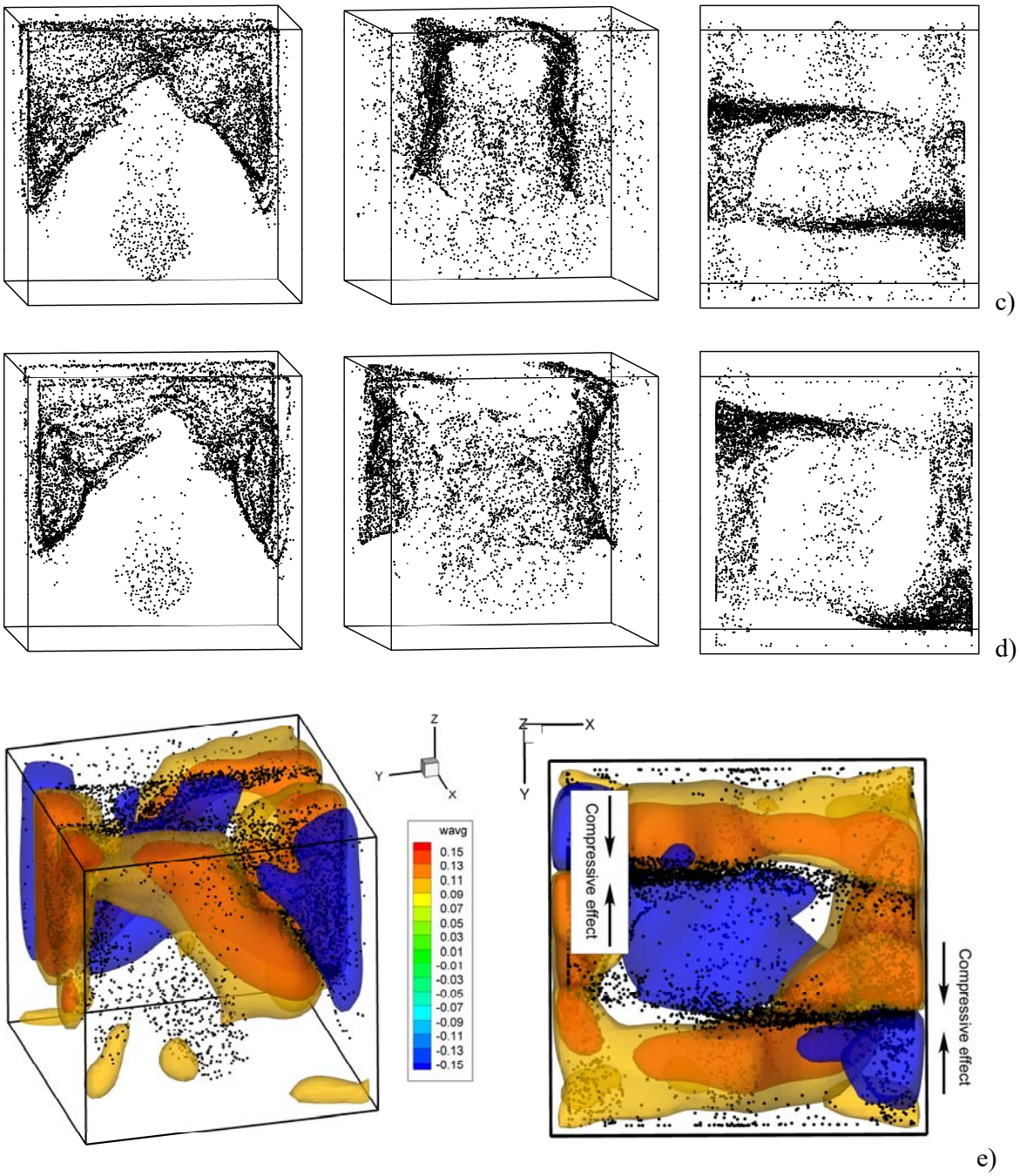

Figure 21: Snapshots (3D views) of particle structures for γ=1x10^8, Ra_ω=10^5, ϖ=5x10^3 (Gs=1220), ξ=2.0 and φ=3.6x10^{-3} (left column: perspective perpendicular to the yz plane, center column: perspective perpendicular to the xz plane, right column: perspective perpendicular to the xy plane): a) t≅3, b) t≅5, c) t≅7, d) t≅10, e) combined 3D view (two different perspectives: perspective perpendicular to the yz plane, and perspective perpendicular to the xy plane) showing particles and isosurfaces of the fluid velocity component in the spanwise direction for t≅7.

The increased interference that dispersed mass has on the spatio-temporal behavior of the fluid-dynamic field is confirmed by the 3D simulations (Figs. 21 and 22). As shown by Fig. 21, an initial transient phase exists where disturbances exhibit a more or less two-dimensional nature, resulting in

the eruption of jets of particles in a direction parallel to the imposed vibrations (Fig. 21a, left panel) already seen in the 2D simulations. At a certain stage, however, the 'curse' of dimensionality starts to affect the dynamics and 3D disturbances tend to be amplified. The related stages of evolution (yet collected in Fig. 21) are extremely interesting.

In particular, as made evident by the views along a direction perpendicular to the xz plane (central panels of Fig. 21), the set/distribution of particles, initially uniformly spread along the spanwise direction, with time tends to split into two main distinct 'swarms'. Initially the two swarms are very close each other (giving the illusion of a single spatially extended bunch of floating particles occupying the center of the cavity, Fig. 21b, central panel). As time passes, however, the two groups of particles come apart (their separation along the x direction tends to increases). This process is accompanied by a reorganization of the dispersed mass, which progressively collapses into two thin accumulation regions stretched in the direction of vibrations, i.e. the y axis (hereafter simply referred to as 'accumulation planes', see Fig. 21c, central panel). The distance between these two planes keeps increasing with time. As a result, the two thin accumulation regions are progressively displaced towards the two walls delimiting the cavity along the x direction. Finally, (when the amount of clear fluid located between the thin accumulation regions and these walls becomes relatively small, i.e. when the accumulation planes occupy a position relatively close to the endwall), the particle-dense regions lose their elongated shape and are turned into two 'blobs' located in opposite corners of the cubic cavity (as seen in the xy plane, Fig. 21d, right panel for t=10). Moreover, an observer looking at the fluid container along the x direction at this time would see triangular-like structures resembling those already found for $\gamma=5\text{x}10^{8}$, $\varpi=10^{4}$, $\xi=0.5$, $\varphi=3.6\text{x}10^{-3}$ (Fig. 21d, left panel).

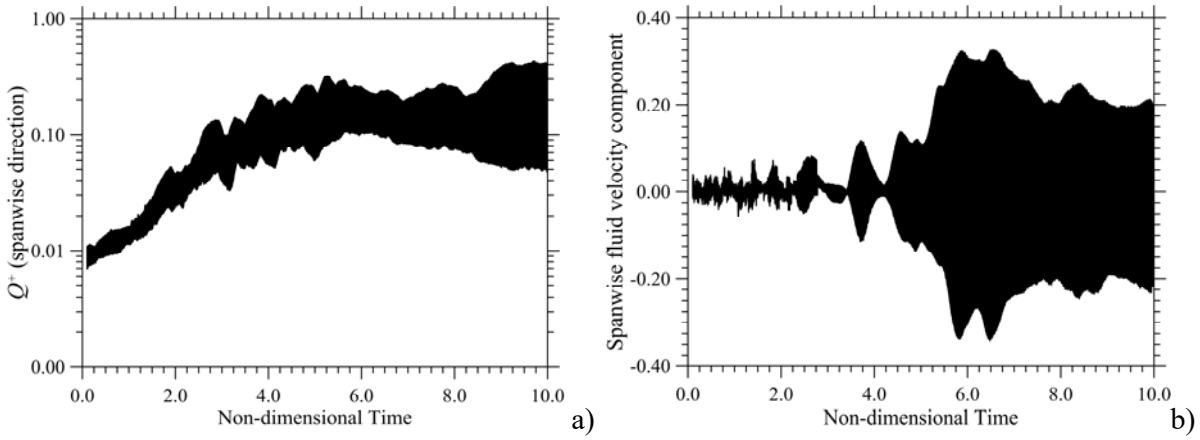

Figure 22: Evolution in time of 3D effects for $\gamma=1\text{x}10^{8}$, $Ra_{\omega}=10^{5}$, $\varpi=5\text{x}10^{3}$ (Gs=1220), $\xi=2.0$ and $\varphi=3.6\text{x}10^{-3}$: a) parameter Q^{+}, b) Fluid velocity component in the spanwise direction probed at the center of the cavity.

Remarkably, this entire process can directly be put in relation with the time-averaged component of fluid velocity in the spanwise direction. As witnessed by Fig. 21e, indeed, it is the time-averaged component induced by the transfer of momentum from particles to fluid that exerts a *compressive action on the particles forcing them to cluster into regions of limited extension* (small thickness) along the spanwise direction and determining the progressive displacement of these particle-dense regions towards the external walls.

Having completed a sketch of the potential impact of the acceleration amplitude (γ), the particle volume fraction (φ), the particle-to-fluid density ratio (ξ) (and therefore the mass load $\chi=\xi\varphi$), we now turn to assessing the role of the last influential factor, that is the Rayleigh number (Ra_ω).

While the previous parameters were all directly affecting solid matter dispersed in the fluid, this number will be exerting an influence on the dynamics following a different cause-and-effect connection, i.e. due to its direct relationship with the *motion of fluid*. A decrease in this number will clearly produce a mitigation of the fluid flow strength and therefore weakening of the inertial forces at play in the considered dynamics.

For the same values of ξ, φ and γ used for the simulations reported in Fig. 21 (namely $\xi=2$, $\varphi=3.6\text{x}10^{-3}$ and $\gamma=1\text{x}10^{8}$), consideration of smaller values of Rayleigh number and angular frequency ($Ra_\omega = 10^4$ and $\varpi=10^3$, respectively) can have (as expected) remarkable beneficial effects on the regularity and perfection of the emerging structures (Figs. 23-24). Although some 3D disturbances can still grow (Fig. 23), particles can successfully reveal the perfection of the underlying attractors (Fig. 24).

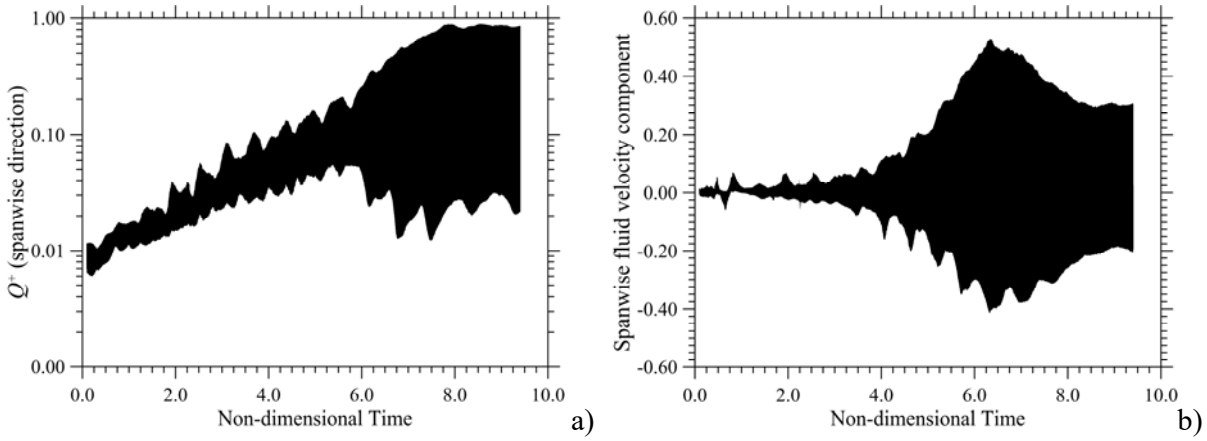

Figure 23: Evolution in time of 3D effects for $\gamma=1\text{x}10^{8}$, $Ra_\omega=10^4$, $\varpi=1\text{x}10^{3}$ (Gs=305), $\xi=2.0$ and $\varphi=3.6\text{x}10^{-3}$: a) parameter Q^+, b) Fluid velocity component in the spanwise direction probed in the center of the cubic cavity.

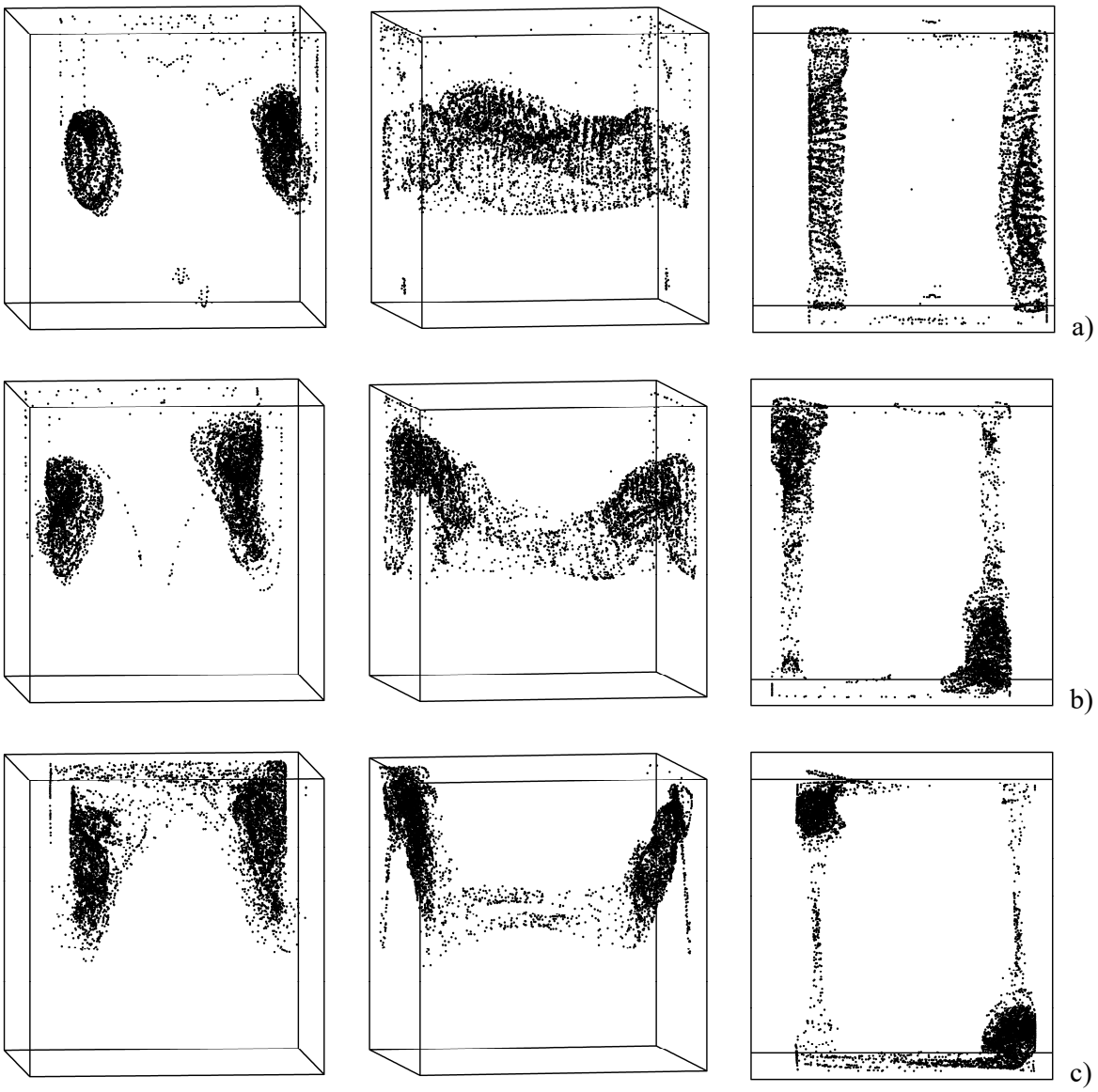

Fig. 24 – continued (see next page for figure caption)

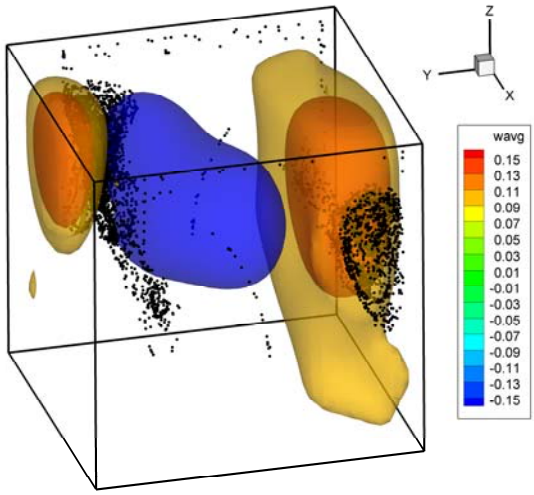

d)

Figure 24: Snapshots (3D views) of particle structures for γ=1x10^8, Ra_ω=10^4, ϖ=10^3 (Gs=305), ξ=2.0 and φ=3.6x10^{-3} (left column: perspective perpendicular to the yz plane, center column: perspective perpendicular to the xz plane, right column: perspective perpendicular to the xy plane): a) t≅5, b) t≅7, c) t≅9, d) Combined 3D view showing particles and isosurfaces of the fluid velocity component in the spanwise direction for t≅7.

Interestingly, the particle distribution reorganization process follows a slightly different evolution path in this situation. Like the case discussed before (γ=1x10^8, Ra_ω=10^5, ϖ=5x10^3, ξ=2.0 and φ=3.6x10^{-3}), as time passes, the initially continuous distribution of particles along the spanwise direction is broken into two different patches (the entire process may give the observer the illusion of a 'cellular mitosis', as evident in Fig. 24b, central panel). The formation of disjoint accumulation regions spanning the entire extension of the cavity in the direction of vibrations, however, does not occur in this case. The particle-dense regions are not stretched in the y direction. Rather, as a result of the entire process, two opposing *blobs* of particles emerge directly. As shown in Fig. 24c (right panel), each blob tends to occupy the corner between one of the walls limiting the cavity in the spanwise direction and another wall limiting it in the direction of vibrations. These two compact accumulation regions are mirror symmetric with respect to the diagonal direction x=y.

As a concluding remark for this section, Figs. 25 and 26 witness that, in line with the various interpretations elaborated before, disturbances can be further mitigated by decreasing the density ratio. For γ = 10^8, ϖ=10^3, Ra_ω = 10^4 and ξ=0.5, particle structures can again manifest as geometrically perfect entities mirroring in the physical space the perfection of the corresponding attractors existing in the 1-way coupled space of phases.

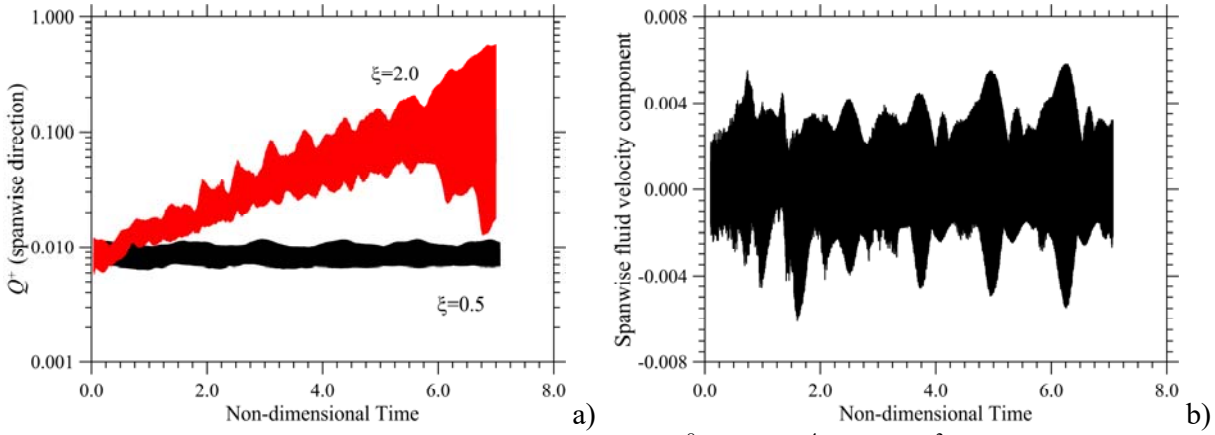

Figure 25: Evolution in time of 3D effects for γ=1x10^8, Ra_ω=10^4, ϖ=1x10^3 (Gs=305), ξ=0.5 and φ=3.6x10^{-3}: a) parameter Q^+, b) Fluid velocity component in the spanwise direction probed in the center of the cubic cavity.

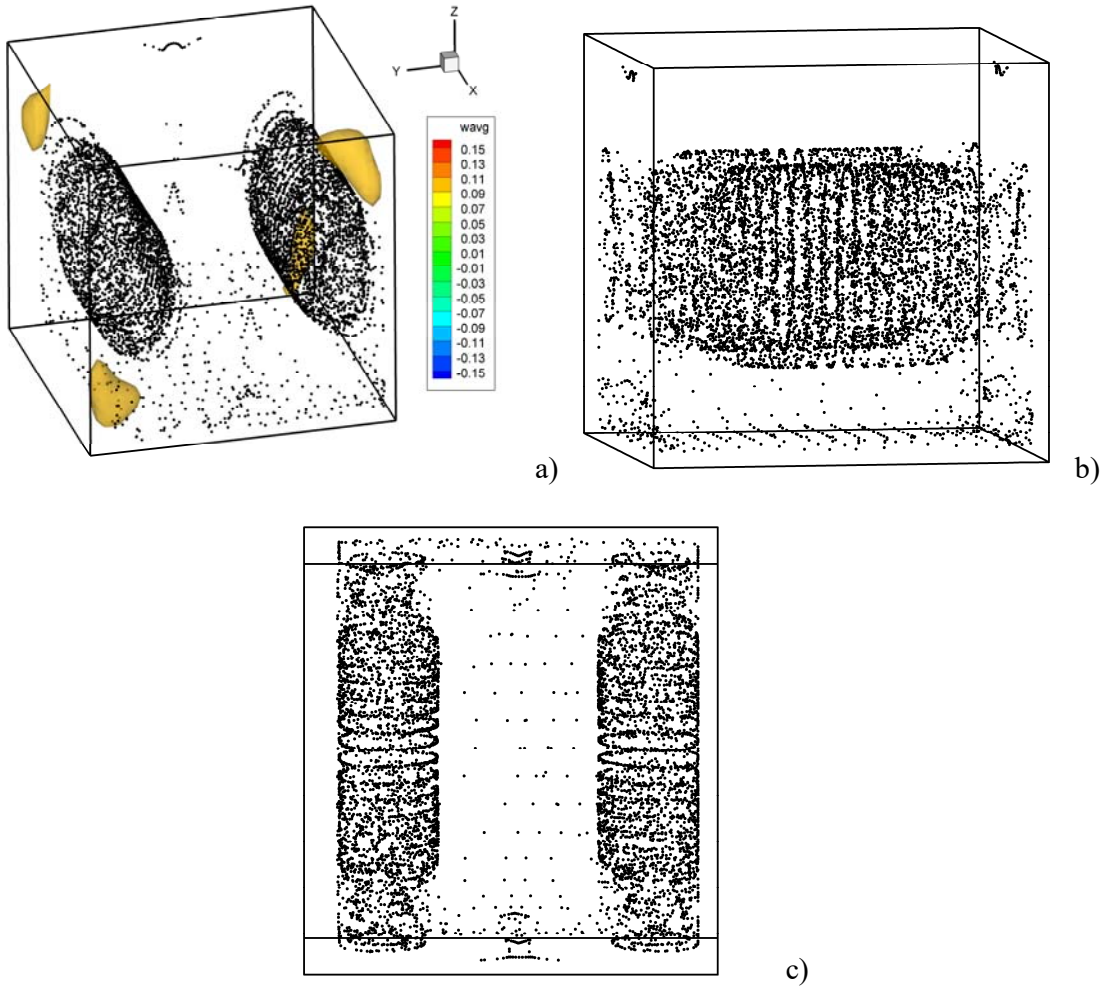

Figure 26: Snapshot (3D views for t≅7) of particle structures for γ=1x10^8, Ra_ω=10^4, ϖ=10^3 (Gs=305), ξ=0.5 and φ=3.6x10^{-3}: a) combined 3D view showing particles and isosurfaces of the fluid velocity component in the spanwise direction, b) view perpendicular to the xz plane, c) view perpendicular to the xy plane).

5. Conclusions

In earlier studies, the relationship between 'particle attractee' and thermovibrational flow has been investigated under the assumption of one-way coupling (which means that attractors have been determined as abstract entities playing the role of "templates" for the accumulation of passively transported inertial particles). Stripped to its basics, the present research scheme has envisioned a parametric investigation aimed to identify the conditions where these ideal entities can still manifest in the form of recognizable particle structures (with a more or less high degree of perfection) if the assumption of dilute dispersion ceases to be valid.

At present there are no published papers examining this issue; hence, this is the first time that detailed data on the related phenomenology (morphology and range of existence of the structures, 3D velocity disturbance growth rates and eventually complete transition to chaotic states) have been presented.

Starting from the realization that earlier models used to address this problem had to be modified to allow for realistic particle structures to exist, the first objective of this work was to pursue modeling of a more complete and sophisticated theoretical and numerical framework. This has been achieved by properly coupling Eulerian (for fluid flow) and Lagrangian (for particle tracking) approaches in such a way to allow realistic inter-phase feedback effects.

Besides purely mathematical and numerical aspects, we have implemented a specific analysis hierarchy by which the problem has partially been tackled under the unphysical constraint of two-dimensional flow. These simulations have successfully been used as a workhorse to test the efficacy of two-way coupled dispersed particles *in disturbing* the carrier fluid flow. In particular, under this constraint, circumstances have been revealed where the back influence of dispersed solid mass on the carrier flow can even *overshadow the underlying attractors* (predicted on the basis of one-way coupling studies) and *lead to completely chaotic particle dy*namics.

Remarkably, the 2D study has also been instrumental in unraveling interwoven or overshadowed processes, which would have otherwise been difficult to interpret, such as the unexpected rupture of symmetry occurring in the spanwise direction.

Using a synergetic combination of 2D and 3D computations, we have conducted an analysis of the triadic relationship among the intensity of fluid convection, the amplitude of acceleration and the frequency of the vibrations. Notably, this interplay takes place within an interlocking ensemble of mutual interferences, where the primary relationship between the fluid flow and its ability to transport the particles (depending on their geometrical and physical properties, i.e. the Stokes number and density ratio) is mediated by the secondary influence that they have on the underlying fluid flow (where also the particle volume fraction starts to play a significant role), as well as the tertiary influence that the flow disturbed in such a way, in turn, has on the particles.

In turn, the tertiary influence encompasses a new category of three-dimensional bifurcations. These are responsible for the emergence of a velocity component along the spanwise direction. This kind of instability is essentially driven by the momentum exchange between fluid and particles and the

ability of the latter to energize the carrier flow. In this regard, this process may be regarded as a new (inertial) mechanism able to produce symmetry breaking phenomena, which have nothing to do with the equivalent ones induced by the time-averaged flow when the Gershuni number is relatively high (effects which would be present even in the complete absence of dispersed particles, see, e.g., Lappa and Burel[64]).

In order to obtain an indirect proof of such conceptual scenario, we have intentionally kept the value of the Gershuni number relatively small and changed the parameters potentially influencing the inter-phase exchange of momentum, namely the Rayleigh number, the acceleration amplitude and the particle density and volume fraction. Such analysis has led to the conclusion that while the 3D instability can be promoted by an increase in the density ratio and/or the particle volume fraction, vice versa a decrease in the acceleration amplitude and/or Rayleigh number can stabilize the carrier flow.

Discerning the role played by the effective percentage of mass dispersed in the fluid has contributed to our understanding of these dynamics and to the capacity to optimize future experiments planned for execution onboard the International Space Station. Perhaps most important of all has been the identification of new routes to as-yet unknown phenomena. We have shown that, as a result of the above-mentioned 3D instabilities, new types of structures can be formed, which differ from those reported in earlier work on the subject due to their prevailing triangular morphology (as seen by an observer taking a look at the flow along a direction perpendicular to the plane of vibrations and imposed temperature difference) and owing to their ability to collapse in planes of accumulation or 'blobs' well separated along the spanwise direction.

Future studies shall be devoted to the investigation of all these dynamics when two different mechanisms are at play at the same time and determine 3D flow, namely the phenomena of purely fluid-dynamic nature that are produced when the Gershuni number takes relatively high values (able to break the symmetry of the quadrupolar field and produce significant values of the time-averaged velocity component in the spanwise direction[64]) and the 3D bifurcations driven by fluid-particle (two-way) momentum transfer revealed by the present work.

Acknowledgments

This work has been supported by the UK Space Agency (STFC grants ST/S006354/1, ST/V005588/1, ST/W002256/1 and ST/W007185/1) in the framework of the PARTICLE VIBRATION (T-PAOLA) project. The author would like to thank Dr. Thomas Burel for the additional simulations presented in Sect. 3.2 conducted using the ANSYS Fluent computational platform and Alessio Boaro for computing the spectra shown in Figs. 5c and 9c.

Data availability

The data that support the findings of this study are openly available in Pure, at https://doi.org/10.15129/b70c149c-04f2-47a6-b23d-50baa35da491

References

[01] Schwabe D. and Mizev A. I., (2011), Particles of different density in thermocapillary liquid bridges under the action of travelling and standing hydrothermal waves, *Eur. Phys. J. Spec. Top.* 192, 13–27.
[02] Gotoda M., Sano T., Kaneko T., and Ueno I., (2015), Evaluation of existence region and formation time of particle accumulation structure (PAS) in half-zone liquid bridge, *Eur. Phys. J. Special Topics*, 224, 299.
[03] Melnikov D.E. and Shevtsova V., (2017), Different types of Lagrangian coherent structures formed by solid particles in three-dimensional time-periodic flows, *European Physical Journal*: Special Topics, 226(6): 1239-1251
[04] Adams F. C. and Watkins R., (1995), Vortices in circumstellar disks*, The Astrophysical Journal*, 451, 314-327.
[05] Lappa M., (2016a), On the nature, formation and diversity of particulate coherent structures in Microgravity Conditions and their relevance to materials science and problems of Astrophysical interest, *Geophysical and Astrophysical Fluid Dynamics*, 110(4): 348-386.
[06] Knez Z., Hrnčič M.K., and Škerget M., (2015), Particle Formation and Product Formulation Using Supercritical Fluids, *Annual Review of Chemical and Biomolecular Engineering*, Vol. 6:379-407
[07] Wang T. and Xing Z., (2014), A fluid-particle interaction method for blood flow with special emphasis on red blood cell aggregation, *Bio-medical materials and engineering*, 24. 2511-7. 10.3233/BME-141065.
[08] Lappa M., (2011), A theoretical and numerical multiscale framework for the analysis of pattern formation in protein crystal engineering, *Journal for Multiscale Computational Engineering*, 9 (2): 149–174.
[09] Saeedi E., Abbasi S., Bohringer K.F. and Parviz B.A., (2006), Molten-Alloy Driven Self-Assembly for Nano and Micro Scale System Integration, *Fluid Dynamics and Materials Processing*, 2(4), 221-246.
[10] Saghir M. Z. and Mohamed A., (2018), Effectiveness in incorporating Brownian and thermophoresis effects in modelling convective flow of water-Al_2O_3 nanoparticles, *Int. J. Numer. Methods Heat Fluid Flow* 28(1), 47–63.
[11] Aksouh M., Chemini R., Mataoui A., Poncet S., (2020), Buoyancy-driven instabilities and particle deposition in a Taylor-Couette apparatus, *International Communications in Heat and Mass Transfer*, 113, 104518.
[12] Bürger R. and Wendland W.L., (2001), Sedimentation and suspension flows: Historical perspective and some recent developments, *Journal of Engineering Mathematics*, 41, 101–116.
[13] Matas J.-P., Morris J.F. and Guazzelli É., (2003), "Transition to Turbulence in Particulate Pipe Flow", *Phys. Rev. Lett*., 90, 014501.
[14] Lashgari I., Picanoa F., Brandt L., (2015), "Transition and self-sustained turbulence in dilute suspensions of finite-size particles", *Theoretical and Applied Mechanics Letters*, 5(3): 121-125.
[15] Lappa M., (2019a), "On the Nature of Fluid-dynamics", Chapter 1 (pp. 1-64) in Understanding the Nature of Science, Patrick Lindholm Editor, Nova Science Publishers Inc., Series: Science, Evolution and Creationism, BISAC: SCI034000, ISBN: 978-1-53616-016-1, https://novapublishers.com/shop/understanding-the-nature-of-science/
[16] Eaton J.K. and Fessler J.R., Preferential concentration of particles by turbulence, *Int. J. Multiphase Flow*, 20, 169-209.
[17] Saw E. W., Shaw R. A., Ayyalasomayajula S., Chuang P. Y., and Gylfason A., (2008), Inertial Clustering of Particles in High-Reynolds-Number Turbulence, *Phys. Rev. Lett*., 100, 214501.
[18] Bragg A. D., (2017), Developments and difficulties in predicting the relative velocities of inertial particles at the small-scales of turbulence, *Phys. Fluids,* 29, 043301.

[19] Shim J. and You D., (2021), Effects of the path history on inertial particle pair dynamics in the dissipation range of homogeneous isotropic turbulence, *Physics of Fluids*, 34, 025104
[20] Yarin A. L., Kowalewski T. A., Hiller W. J., and Koch St., (1996), Distribution of particles suspended in convective flow in differentially heated cavity, *Physics of Fluids*, 8, 1130-1140.
[21] Tanaka S., Kawamura H., Ueno I., and Schwabe D., (2006), Flow structure and dynamic particle accumulation in thermocapillary convection in a liquid bridge, Phys. Fluids, 18, 067103.
[22] Schwabe D., Mizev A.I., Udhayasankar M. and Tanaka S., (2007), Formation of dynamic particle accumulation structures in oscillatory thermocapillary flow in liquid bridges, *Phys. Fluids*, 19(7), 072102.
[23] Ueno I., Abe Y., Noguchi K., and Kawamura H., (2008), Dynamic particle accumulation structure (PAS) in half-zone liquid bridge – Reconstruction of particle motion by 3-D PTV, Adv. Space Res., 41(12), 2145-2149.
[24] Pushkin D., Melnikov D., Shevtsova V., (2011), Ordering of Small Particles in One-Dimensional Coherent Structures by Time-Periodic Flows, *Phys. Rev. Lett.*, 106, 234501.
[25] Melnikov D.E., Pushkin D.O., Shevtsova V.M., (2013), Synchronization of finite-size particles by a traveling wave in a cylindrical flow, *Phys Fluids*, 25 (9), 092108
[26] Gotoda M., Melnikov D. E., Ueno I., and Shevtsova V., (2016), Experimental study on dynamics of coherent structures formed by inertial solid, particles in three-dimensional periodic flows, *Chaos*, 26, 073106 (11 pages).
[27] Toyama A., Gotoda M. , Kaneko T., Ueno I., (2017), Existence Conditions and Formation Process of Second Type of Spiral Loop Particle Accumulation Structure (SL-2 PAS) in Half-zone Liquid Bridge, Microgravity Sci. Technol., 29:263–274.
[28] Lappa M., (2013a), Assessment of the role of axial vorticity in the formation of Particle Accumulation Structures (PAS) in supercritical Marangoni and hybrid thermocapillary-rotation-driven flows, *Phys. Fluids,* 25(1) 012101 (11 pages).
[29] Lappa M., (2013b), On the Existence and Multiplicity of One-dimensional Solid Particle Attractors in Time-dependent Rayleigh-Bénard Convection, *Chaos*, 23(1), 013105 (9 pages).
[30] Lappa M., (2013c), On the variety of particle accumulation structures under the effect of gjitters, *J. Fluid Mech*., 726, 160-195.
[31] Lappa M., (2014a), Stationary Solid Particle Attractors in Standing Waves, *Phys. Fluids,* 26(1), 013305 (12 pages).
[32] Metcalfe G., (2019), Push and pull: attractors and repellors of a dynamical system can localize inertial particles, *Granular Matter*, 21, 95. https://doi.org/10.1007/s10035-019-0949-8
[33] Venditti C., Giona M. and Adrover A. (2022), Invariant manifold approach for quantifying the dynamics of highly inertial particles in steady and time-periodic incompressible flows, *Chaos* 32, 023121
[34] Sommerfeld M., (1990), Particle Dispersion in Turbulent Flow: The effect of particle size distribution, 7(1-4), 209-220.
[35] Lyubimov D.V., Lyubimova T.P., Straube A.V., (2005), Accumulation of Solid Particles in Convective Flows, *Microgravity Sci. Technol*., XVI – I, 210-214.
[36] Haller G. and Sapsis T., (2008), Where do inertial particles go in fluid flows?, *Physica D* 237(5), 573–583.
[37] Capobianchi P. and Lappa M., (2020), Particle accumulation structures in noncylindrical liquid bridges under microgravity conditions, *Physical Review Fluids*, 5(8), 084304 (30 pages).
[38] Capobianchi P. and Lappa M., (2021a), On the influence of gravity on particle accumulation structures in high aspect-ratio liquid bridges, *Journal of Fluid Mechanics*, Volume 908, 10 February 2021 , A29 (30 pages).
[39] Rossing T. D. , (1982), Chladni's Law for Vibrating Plates, *American Journal of Physics*, 50, 271–274.

[40] Capobianchi P. and Lappa M., (2021b), Particle accumulation structures in a 5 cSt silicone oil liquid bridge: New data for the preparation of the JEREMI Experiment, *Microgravity Science & Technology*, 33, 31 (12 pages).
[41] Gershuni G.Z. and Lyubimov D.V.,(1998), Thermal Vibrational Convection Wiley, England.
[42] Savino R. and Lappa M., (2003), "Assessment of the thermovibrational theory: application to g-jitter on the Space-station", *Journal of Spacecraft and Rockets*, 40 (2), 201-210.
[43] Mialdun A., Ryzhkov I.I., Melnikov D.E., and Shevtsova V., (2008), Experimental Evidence of Thermal Vibrational Convection in a Nonuniformly Heated Fluid in a Reduced Gravity Environment, *Phys. Rev. Lett*., 101, 084501.
[44] Ahadi A.H. and Saghir M.Z., (2012), Quasi Steady State Effect of Micro Vibration from Two Space Vehicles on Mixture During Thermodiffusion Experiment, *Fluid Dynamics & Materials Processing*, Vol.8, No.4, 2012, pp.397-422, doi:10.3970/fdmp.2012.008.397
[45] Lyubimova T.P., Perminov A.V., Kazimardanov M.G. (2019), Stability of quasi-equilibrium states and supercritical regimes of thermal vibrational convection of a Williamson fluid in zero gravity conditions, *Int. J. Heat Mass Transf*., 129, 406-414.
[46] Bouarab S., Mokhtari F., Kaddeche S., Henry D., Botton V., and Medelfef1 A., (2019), Theoretical and numerical study on high frequency vibrational convection: Influence of the vibration direction on the flow structure, *Phys. Fluids*, 31(4), 043605
[47] Shevtsova V., Lyubimova T., Saghir Z., Melnikov D., Gaponenko Y., Sechenyh V., Legros J. C., and Mialdun A., (2011), "IVIDIL: On-board g-jitters and diffusion controlled phenomena," *J. Phys.: Conf. Ser.* 327, 012031.
[48] Shevtsova V., Mialdun A., Melnikov D., Ryzhkov I., Gaponenko Y., Saghir Z., Lyubimova T., and Legros J. C., (2011), "The IVIDIL experiment onboard the ISS: Thermodiffusion in the presence of controlled vibrations," *Compt. Rend. Mécaniq*. 339(5), 310–317.
[49] Maryshev B., Lyubimova T., and Lyubimov D., (2013), "Two-dimensional thermal convection in porous enclosure subjected to the horizontal seepage and gravity modulation," *Phys. Fluids* 25, 084105.
[50] Lappa M., (2016b), Control of convection patterning and intensity in shallow cavities by harmonic vibrations, *Microgravity Science & Technology*, 28(1): 29-39.
[51] Vorobev A. and Lyubimova T., (2019), Vibrational convection in a heterogeneous binary mixture. Part I. Time-averaged equations, *J. Fluid Mech*., 870, 543-562.
[52] Boaro A. and Lappa M., (2021a), Multicellular States of Viscoelastic Thermovibrational Convection in a Square Cavity, *Physics of Fluids*, 33(3), 033105 (18 pages).
[53] Boaro A. and Lappa M., (2021b), Competition of overstability and stabilizing effects in viscoelastic thermovibrational flow, *Phys. Rev E*, 104 (2), 025102 (17 pages).
[54] Crewdson G. and Lappa M., (2021), The zoo of modes of convection in liquids vibrated along the direction of the temperature gradient, *FLUIDS*, 6(1), 30 (23 pages). https://www.mdpi.com/2311-5521/6/1/30
[55] Crewdson G. and Lappa M., (2022a), Spatial and temporal evolution of three-dimensional thermovibrational convection in a cubic cavity with various thermal boundary conditions, *Physics of Fluids*, 34(1), 014108, 21 pages.
[56] Lappa M., (2014b), The patterning behaviour and accumulation of spherical particles in a vibrated non-isothermal liquid, *Phys. Fluids*, 26(9), 093301.
[57] Lappa M., (2016c), Numerical study into the morphology and formation mechanisms of three-dimensional particle structures in vibrated cylindrical cavities with various heating conditions, *Physical Review Fluids*, 1(6), 064203.
[58] Lappa M., (2017), On the multiplicity and symmetry of particle attractors in confined non-isothermal fluids subjected to inclined vibrations, *Int. J. Multiphase Flow*, 93, 71-83.
[59] Lappa M., (2019b), On the formation and morphology of coherent particulate structures in non-isothermal enclosures subjected to rotating g-jitters, *Phys. Fluids*, 31(7), 073303 (11 pages).

[60] Tabakova S.S. and Zapruanov Z.D., (1982), On the hydrodynamic interaction of two spheres oscillating in a viscous fluid. I. Axisymmetrical case. *J. Appl. Math. Phys*. (ZAMP), 33, 344–357 - II. Three dimensional case. *J. Appl. Math. Phys*. (ZAMP), 33,487–502.
[61] Wunenburger R., Carrier V., and Garrabos Y., (2002), Periodic order induced by horizontal vibrations in a two-dimensional assembly of heavy beads in water, *Phys. Fluids*, 14(7), 2350-2359.
[62] Ivanova A.A., Kozlov V.G. and Kuzaev A.F., (2005), Vibrational lift force acting on a body in a fluid near a solid surface. *Dokladi RAN*, vol. 402 (4), pp. 1–4 (Translated: Doklady Physics, vol. 50 (6), pp. 311–314).
[63] Kozlov V.G., Ivanova A.A. and Evesque P., (2006), Block stratification of sedimenting granular matter in a vessel due to vertical vibration, *Fluid Dyn. Mater. Process*., 2(3), 203-210.
[64] Lappa M. and Burel T., (2020), Symmetry Breaking Phenomena in Thermovibrationally Driven Particle Accumulation Structures, *Phys. Fluids*, 32(5), 053314 (23 pages).
[65] Crewdson G. and Lappa M., (2022b), An investigation into the behavior of non-isodense particles in chaotic thermovibrational flow, *Fluid Dynamics & Materials Processing*, 18(3), Accepted for publication on 15 Nov 2021. DOI: 10.32604/fdmp.2022.020248
[66] Lappa M., Burel T., Kerr M., Crewdson G., Boaro A., Capobianchi P., Bonnieu, S.V., Murphy L., Randall P. and Hens S., (2022), Particle Vibration, an instrument to study particle accumulation structures on board the International Space Station, *Microgravity Science and Technology,* DOI: 10.1007/s12217-022-09939-2, *To appear*.
[67] Uchiyama T., (2011), Grid-Free Vortex Method for Particle-Laden Gas Flow, *Fluid Dyn. Mater. Process*., 7(4), 371-388.
[68] Bothe D., Kröger M. and Warnecke H.-J. (2011), A VOF-Based Conservative Method for the Simulation of Reactive Mass Transfer from Rising Bubbles, *Fluid Dyn. Mater. Process*., 7(3), 303-316.
[69] Mark A., Rundqvist R. and Edelvik F., (2011), Comparison Between Different Immersed Boundary Conditions for Simulation of Complex Fluid Flows, *Fluid Dyn. Mater. Process*., 7(3), 241-258
[70] Homma S., Yokotsuka M., Tanaka T., Moriguchi K., Koga J. and Tryggvason G., (2011), Numerical Simulation of an Axisymmetric Compound Droplet by Three-Fluid Front-Tracking Method, *Fluid Dyn. Mater. Process*., 7(3), 231-240.
[71] Haeri S. and Shrimpton J.S., (2014), Fully resolved simulation of particle deposition and heat transfer in a differentially heated cavity, *Int. J. Heat Fluid Flow*, 50, 1-15.
[72] Lappa M., Drikakis D., Kokkinakis I., (2017), On the propagation and multiple reflections of a blast wave travelling through a dusty gas in a closed box, *Physics of Fluids*, 29(3), 033301 (19 pages).
[73] Maxey M. R. and Riley J. J., (1983), Equation of motion for a small rigid sphere in a nonuniform flow, *Phys. Fluids*, 26, 883-889.
[74] Kuhlmann H.C. et al. (2014), The JEREMI-Project on thermocapillary convection in liquid bridges. Part A: Overview of Particle Accumulation Structures, *Fluid Dyn. Mater. Process*., 10 (1), 1-36.
[75] Clift R, Grace J.R, Weber M.E., (1978), Bubbles, Drops, and Particles, Academic Press, New York.
[76] Lappa M., (2019c), Time reversibility and non-deterministic behaviour in oscillatorily sheared suspensions of non-interacting particles at high Reynolds numbers, *Computers & Fluids*, 184, 78-90.
[77] Elghobashi, S (1994), On predicting particle-laden turbulent flows. *Appl. Sci. Res.* 52, 309–329.
[78] Bodnár T., Galdi G. P. and Necasová Š., 2017, Particles in Flows. Birkhäuser.
[79] Eaton J.K., (2009), Two-way coupled turbulence simulations of gas-particle flows using point-particle tracking, *International Journal of Multiphase Flow* 35, 792–800.
[80] Bianco V., Chiacchio F., Manca O., Nardini S., (2009), Numerical investigation of nanofluids forced convection in circular tubes, *Applied Thermal Engineering*, 29(17–18), 3632-3642.

[81] Greifzu F., Kratzsch C., Forgber T., Lindner F. and Schwarze R., (2016), Assessment of particle-tracking models for dispersed particle-laden flows implemented in OpenFOAM and ANSYS FLUENT, *Engineering Applications of Computational Fluid Mechanics*, 10:1, 30-43, DOI: 10.1080/19942060.2015.1104266.
[82] Ladyzhenskaya O.A., (1969), The Mathematical Theory of Viscous Incompressible Flow, Gordon and Breach, 2nd Edition, New York - London, 1969.
[83] Shen J., (1996), "On error estimates of the projection methods for the Navier–Stokes equations: Second-order schemes", *Math. Comput*., 65(215): 1039-1066.
[84] Armfield S. and Street R., (1999), "The Fractional-Step Method for the Navier-Stokes Equations on Staggered Grids: The Accuracy of Three Variations", *J. Comput. Phys*., 153(2): 660-665.
[85] Lee M.J., Oh B.D. and Kim Y.B., (2001), "Canonical fractional-step methods and consistent boundary conditions for the incompressible Navier–Stokes equations", *J. Comput. Phys*., 168: 73–100.
[86] Guermond J.-L., Minev P. and Shen J., (2006), "An Overview of Projection Methods for Incompressible Flows. Comput. Methods", *Comput. Methods Appl. Mech. Eng*., 195: 6011-6045.
[87] Choi S.K., Nam H.Y., Cho M. (1994a), Systematic comparison of finite-volume calculation methods with staggered and nonstaggered grid arrangement, *Numer Heat Transfer*, Part B 25 (2): 205–221.
[88] Choi S.K., Nam H.Y., Cho M., (1994b), Use of staggered and nonstaggered grid arrangements for incompressible flow calculations on nonorthogonal grids, *Numer Heat Transfer*, Part B 25(2): 193–204.
[89] Lappa M., (1997), Strategies for parallelizing the three-dimensional Navier-Stokes equations on the Cray T3E, *Science and Supercomputing* at CINECA, 11: 326-340.
[90] Lappa M., (2019d), A mathematical and numerical framework for the simulation of oscillatory buoyancy and Marangoni convection in rectangular cavities with variable cross section, Chapter 12 (pp. 419-458) in *Computational Modeling of Bifurcations and Instabilities in Fluid Mechanics* (Springer Mathematical Series, 2018, Part of the Computational Methods in Applied Sciences book series - COMPUTMETHODS, volume 50), Editor Alexander Gelfgat - ISBN 978-3-319-91493-0. DOI: 10.1007/978-3-319-91494-7.
[91] Patankar S.V., (1981), "Numerical heat transfer and fluid flow", Hemisphere Publishing Corporation,1981.
[92] Rhie C.M. and Chow W.L., (1983), Numerical study of the turbulent flow past an airfoil with trailing edge separation, *AIAA J.,* 21,1525–1532.
[93] Hutchinson B.R. and Raithby G.D., (1986), A multigrid method based on the additive correction strategy, *Numer. Heat Transf*., 9, 511–537.
[94] Cash J. R. and Karp A.H., (1990), A Variable Order Runge-Kutta Method for Initial Value Problems with Rapidly Varying Right-Hand Sides. *ACM Trans. Math. Softw*., 16, 201–222.
[95] Khallouf H., Gershuni G. Z. and Mojtabi A., (1995), "Numerical study of two-dimensional thermo-vibrational convection in rectangular cavities", *Num. Heat Trans*. A, 27: 297-305.
[96] Lappa M. (2009), "Thermal Convection: Patterns, Evolution and Stability", 700 pages, John Wiley & Sons, Ltd (2009, Chichester, England).
[97] Lappa M. and Ferialdi H., (2018), Multiple solutions, Oscillons and Strange Attractors in ThermoViscoElastic Marangoni Convection, *Phys. Fluids*, 30(10), 104104 (19 pages).
[98] Lappa M., (2018), On the transport, segregation and dispersion of heavy and light particles interacting with rising thermal plumes, *Phys. Fluids*, 30(3), 033302 (23 pages).